Universidade de Aveiro
2022

Marcos António Spínola Monteiro Gomes

Desenvolvimento de um modelo do cérebro humano em elementos finitos hexaédricos

Development of a model of the human brain using hexahedral finite elements

Universidade de Aveiro
2022

Marcos António Spínola Monteiro Gomes

Desenvolvimento de um modelo do cérebro humano em elementos finitos hexaédricos

Development of a model of the human brain using hexahedral finite elements

Dissertação apresentada à Universidade de Aveiro para cumprimento dos requisitos necessários à obtenção do grau de Mestre em Engenharia Mecânica, realizada sob orientação científica do Doutor Fábio António Oliveira Fernandes, Professor Auxiliar em Regime Laboral do Departamento de Engenharia Mecânica da Universidade de Aveiro e de Doutor Ricardo José Alves de Sousa, Professor Auxiliar com Agregação do Departamento de Engenharia Mecânica da Universidade de Aveiro.

Thesis presented to the University of Aveiro as a requirement to obtain the Master Degree in Mechanical Engineering, and carried out under the scientific supervision of Doctor Fábio António Oliveira Fernandes, Assistant Professor Under the Portuguese Labour Code at Department of Mechanical Engineering, University of Aveiro and Doctor Ricardo José Alves de Sousa, Assistant Professor at Department of Mechanical Engineering, University of Aveiro.

Esta dissertação teve o apoio financeiro dos projetos UIDB/004 81/2020 e UIDP/00481/2020 - Fundação para a Ciência e a Tecnologia; e CENTRO-01 -0145 FEDER-022083 - Programa Operacional Regional do Centro (Centro2020), através do Portugal 2020 e do Fundo Europeu de Desenvolvimento Regional.

O júri / The jury

Presidente / President

Prof. Doutor Robertt Angelo Fontes Valente
Professor Associado, Universidade de Aveiro

Vogais / Committee

Prof. Doutor Fábio António Oliveira Fernandes
Professor Auxiliar em Regime Laboral, Universidade de Aveiro

Prof. Doutor Marco Paulo Lages Parente
Professor Associado, Faculdade de Engenharia da Universidade do Porto

Agradecimentos / Acknowledgements

Agradeço à minha família e amigos.

Palavras-chave Cérebro, hexaedros, elementos finitos

Resumo As lesões cerebrais são um problema significativo em todo o mundo, em particular nos Estados Unidos da América, onde foram documentadas anualmente 1,7 milhão de lesões. Os testes necessários para esta avaliação são muito complexos.Testes em cadáveres levantam sérias questões de ética, além de testes de colisão 'in vivo' não são viavíes. Neste contexto, há uma grande necessidade de desenvolvimento de modelos de elementos finitos da cabeça humana como o YEAHM, desenvolvido por membros da Universidade de Aveiro. Por esta razão, o objetivo desta dissertação visa melhorar o YEAHM, especialmente os componentes do cérebro, estudando como este se comporta sob diferentes tipos de elementos. A formulação de elementos finitos é de extrema importância para a precisão e eficácia dos modelos. Várias validações foram realizadas, comparando os resultados das simulações com os resultados experimentais. As simulações com elementos hexaédricos, sob condições específicas, obtiveram melhores resultados com um custo computacional inferior.

Keywords Brain, hexahedral, finite element

Abstract

Traumatic brain injury is a significant problem worldwide, particularly in the United States of America, where 1.7 million TBIs are documented annually. The tests required for this assessment are very complex. Tests on cadavers may raise serious ethical questions, and *in-vivo* crash tests are not viable. In this context, there is a great need for developing finite element models of the human head, such as the YEAHM, developed by members of the University of Aveiro. For this reason, this dissertation aims to improve the YEAHM, especially its brain components, by studying how it behaves under different finite element types. The finite element formulation is of utmost importance for the general accuracy and efficiency of the models. Several validations were performed, comparing the simulation results against the experimental results. The simulations with hexahedral elements, under specific conditions, obtained better results with a lower computational cost.

Contents

Contents i

List of Tables ii

List of Figures iii

List of Acronyms vii

List of Symbols ix

1 Introduction 1
- 1.1 Motivation . . . 1
- 1.2 Reading Guide . . . 3

2 State-of-the-art 5
- 2.1 Anatomy of the head . . . 5
  - 2.1.1 Skull . . . 5
  - 2.1.2 Meninges . . . 6
  - 2.1.3 Brain . . . 7
- 2.2 Traumatic brain injuries . . . 13
  - 2.2.1 Focal injuries . . . 14
  - 2.2.2 Diffuse injuries . . . 15
  - 2.2.3 Head injury criteria . . . 16
- 2.3 Finite element head model (FEHM) . . . 16
  - 2.3.1 History of FEHM . . . 17
  - 2.3.2 Comparison between different element types . . . 21
  - 2.3.3 Yet Another Head Model (YEAHM) . . . 22

3 Methodology 29
- 3.1 Geometrical modelling of the brain . . . 29
  - 3.1.1 Model 1 . . . 29
  - 3.1.2 Model 2 . . . 37
- 3.2 Validation methodology . . . 38
  - 3.2.1 Hardy Experiments . . . 38
  - 3.2.2 Nahum Experiments . . . 41
- 3.3 YEAHM assembly + Model 1/Model 2 . . . 43

4 Simulation and results **45**
4.1 Validation 45
4.1.1 Nahum's experiment - Intracranial Pressure simulation results . . . 45
4.1.2 Hardy's Experiment - Brain Motion simulation results 52

5 Conclusion and future work **65**
5.1 Future works 65

Bibliography **67**

List of Tables

2.1 Proposed limits in the literature for brain injury. 16
2.2 Material properties used for the brain in the history of FEHM. 21
2.3 Brain modeling properties. 25
2.4 CSF properties. 25
2.5 BV/SSS properties. 25
2.6 Skull properties. 26
2.7 New skull properties. 26

3.1 Mesh properties of both models. 37

4.1 Comparison between different models element types for Nahum simulations. 49
4.2 Comparison between different models and element types for Hardy simulations. 63

List of Figures

1.1 Estimated Average Annual Numbers of Traumatic Brain Injury-Related causes in USA, 2002-2006. 2

2.1 Composition of the human skull 6
2.2 All visible sutures of the human skull. 6
2.3 Distinction of the Meninges. 7
2.4 Distinct parts composing the brain 8
2.5 Division of the brain in four separate lobes, and their respective position. 9
2.6 Visualization of both hemispheres divided by the Medial longitudinal fissure. 9
2.7 Similar appearance between the cerebrum and the cerebellum. 11
2.8 Brainstem composition. 12
2.9 Stiffness of various organs in human body. 13
2.10 Classifications of traumatic brain injury (TBI). 14
2.11 Difference between Epidural and Subdural Hematomas. 15
2.12 FEHM developed by Hosey. (A) Sagittal cross section; (B) Coronal cross section 17
2.13 FEHM developed by Hosey. (A) Sagittal cross section; (B) Coronal cross section. 18
2.14 The Strasbourg University Finite Element Head Model (SUFEHM). . . . 19
2.15 Kungliga Tekniska Högskolan (KTH) FEHM. (A) skull; (B) brain with bridging veins; (C) cut view of the head and neck model; (D) anatomical structures. 20
2.16 The University College Dublin Brain Trauma Model (UCDBTM). (A) the skull; (B) the brain; (C) cut view illustrating the intracranial content. . . 21
2.17 Solid elements recommendations, adapted from Wang et al. 22
2.18 Methodology used in YEAHM. 22
2.19 Constitution of YEAHM model. Skull (red) with all the sutures (yellow), trabecular bone (white), CSF (blue), brain (green) and the bridging veins (grey). 23
2.20 Post-failure stress-strain curve for both cortical and sutures tissues. 26
2.21 Shear retention model values for both cortical and sutures tissues. 27

3.1 STL file of the brain model imported to hypermesh. 30
3.2 Front, side and top view of the brain model. 31
3.3 Geometry failure, the elements connected between both hemispheres. . . . 32

3.4 Geometry failure, the elements connected between both hemispheres and the cerebellum. . . . 32
3.5 The right hemisphere before running the 'Shrink Wrap Mesh' algorithm, with flattened surfaces in Corpus Callosum and Cerebellum. . . . 33
3.6 The left hemisphere before running the 'Shrink Wrap Mesh' algorithm, with flattened surfaces in Corpus Callosum and Cerebellum. . . . 33
3.7 The Cerebellum before running the 'Shrink Wrap Mesh' algorithm, with flattened surface one the place where it will be connected to both hemispheres. . . . 34
3.8 Front cut view of the brain model. All three components of the brain (blue) and the manual connections (green). . . . 35
3.9 Front cut view of the brain. Grey matter (grey) and white matter (white). 36
3.10 Second model with hexahedral mesh built by using the algorithm 'split'. 37
3.11 The inverted, head suspension fixture. . . . 38
3.12 NDTs columns location used in Hardy experiments. . . . 39
3.13 Displacement time histories for NDTs locations in the X direction for test C755-T2. . . . 39
3.14 Displacement time histories for NDTs locations in the Z-direction for test C755-T2. . . . 40
3.15 Rotational acceleration from C755-T2 experiment. . . . 40
3.16 Translational acceleration from C755-T2 experiment 41
3.17 Configuration of Nahum experiment for model validation. . . . 41
3.18 Pressure values from Experiment 37. . . . 42
3.19 Side cut-view of the final assembly containing the skull (grey), CSF (red) and Model 1 (green). . . . 43

4.1 Comparison of frontal pressure between experimental and numerical results. 46
4.2 Comparison of parietal pressure between experimental and numerical results. 46
4.3 Comparison of ocipital pressure between experimental and numerical results. 47
4.4 Comparison of ocipital pressure between experimental and numerical results. 47
4.5 Comparison of fossa pressure between experimental and numerical results. 48
4.6 Pressure values obtained in the brain surface 50
4.7 Representation of Coup phenomenon obtained by Model 1 with C3D8R . 50
4.8 Representation of Countreoup phenomenon obtained by Model 1 with C3D8R 51
4.9 Side cut-view of the skull, showing the new coordinate system. . . . 52
4.10 Comparison of displacement-time histories, measured at a1 in the X-direction, between experimental and numerical results. . . . 53
4.11 Comparison of displacement-time histories, measured at a2 in the X-direction, between experimental and numerical results. . . . 53
4.12 Comparison of displacement-time histories, measured at a3 in the X-direction, between experimental and numerical results. . . . 54
4.13 Comparison of displacement-time histories, measured at a4 in the X-direction, between experimental and numerical results. . . . 54
4.14 Comparison of displacement-time histories, measured at a5 in the X-direction, between experimental and numerical results. . . . 55

4.15 Comparison of displacement-time histories, measured at a1 in the Z-direction, between experimental and numerical results. 55
4.16 Comparison of displacement-time histories, measured at a2 in the Z-direction, between experimental and numerical results. 56
4.17 Comparison of displacement-time histories, measured at a3 in the Z-direction, between experimental and numerical results. 56
4.18 Comparison of displacement-time histories, measured at a4 in the Z direction, between experimental and numerical results. 57
4.19 Comparison of displacement-time histories, measured at a5 in the Z-direction, between experimental and numerical results. 57
4.20 Comparison of displacement-time histories, measured at p1 in the X-direction, between experimental and numerical results. 58
4.21 Comparison of displacement-time histories, measured at p2 in the X-direction, between experimental and numerical results. 58
4.22 Comparison of displacement-time histories, measured at p3 in the X-direction, between experimental and numerical results. 59
4.23 Comparison of displacement-time histories, measured at p4 in the X-direction, between experimental and numerical results. 59
4.24 Comparison of displacement-time histories, measured at p5 in the X-direction, between experimental and numerical results. 60
4.25 Comparison of displacement-time histories, measured at p1 in the Z-direction, between experimental and numerical results. 60
4.26 Comparison of displacement-time histories, measured at p2 in the Z-direction, between experimental and numerical results. 61
4.27 Comparison of displacement-time histories, measured at p3 in the Z-direction, between experimental and numerical results. 61
4.28 Comparison of displacement-time histories, measured at p4 in the Z-direction, between experimental and numerical results. 62
4.29 Comparison of displacement-time histories, measured at p5 in the Z-direction, between experimental and numerical results. 62

List of Acronyms

BV	Bridging Veins
FEM	Finite Element Method
FEHM	Finite Element Head Model
GSI	Gadd Severity Index
HIC	Head Injury Criteria
EDH	Epidural Hematoma
SDH	Subdural Haematoma
ICH	Intracerebral Hematomas
SSS	Superior Sagittal Sinus
TBI	Traumatic Brain Injury
YEAHM	Yet Another Head Model
CNS	Central nervous system
WSUHIM	Wayne State University Brain Injury Model
SUFEHM	Strasbourg University Finite Element Head Model
KTH	Kungliga Tekniska Högskolan
UCDBTM	University College Dublin Brain Trauma Model
CSF	Cerebrospinal fluid
STL	Stereolithography
DAI	Diffuse axonal injury
NDT	Neural-Density Target
HIP	Head Impact Power
WSTC	Wayne State Tolerance Curve

List of Symbols

K	Bulk modulus
ρ	Density
ν	Poisson's ratio
G_∞	Long Term Shear modulus
G_0	Short Term Shear modulus
$C10, C01$	Material parameters
$D1, \alpha 1$	Material parameters
E	Young's modulus
β	Decay factor
μ	Shear modulus
g_1, g_2	Relaxation coefficients
τ_1, τ_2	Characteristic relaxation times

Chapter 1

Introduction

In this chapter the motivation for the work developed is presented

1.1 Motivation

The most common and the most severe form of trauma related injury is a head injury, due to its mortality rate compared to trauma without head injury. Not only does this account for a high mortality rate but also a much higher lifelong disability rate, making it a serious public health problem with significant social and economic costs. The most relevant head injury in terms of mortality rate is Traumatic brain injury (TBI) since they directly affect the brain. In the United States of America, there are 1.7 million documented TBI annually, distributed over all types of causes as can be seen in figure 1.1 [1; 2].

To reduce the risk of fatal injuries, it is important to study the head completely, as this is where the brain is located. Due to moral and ethical principles, it is not possible to carry out tests on living beings, so it was necessary to find a sustainable solution. Simulations based on the Finite Element Method (FEM) were developed, which is a better cost-effective method to predict possible head injuries than using human simulacra or dummies.

The construction of head models using FEM opens up several possibilities for predicting brain injury. Using Finite Element Head Models (FEHM), it is possible to compute variables such as stress and strain that would not be feasible experimentally (measuring *in vivo*). Another reason that FEHM is considered a valuable tool is that it can be used in the development of protective equipment and in the reconstruction of injury events by predicting brain injury under impact conditions.

Over the years many FEHM have been developed by different authors. One of them is the Yet Another Head Model (YEAHM), developed and validated by Fernandes et al. [3] and further enhanced by former students of the Mechanical Department of the University of Aveiro. To obtain reliable results, the finite element model must be as real-

istic as possible. In this particular case, the YEAHM brain is modeled with tetrahedral elements. There is a virtual stiffness associated with this type of element that is problematic when modeling incompressible tissues/materials, and the brain is one of these cases. Therefore, the present work aims to create a hexahedral mesh for the brain. Since the generation of meshes with hexahedral elements is extremely complex, especially for complex geometries, one of the goals is to test different strategies to obtain a solution with good results at the lowest possible computational cost. Subsequently, the brain model will be segmented by gray and white matters.

CAUSE	EMERGENCY DEPARTMENT VISITS	HOSPITALIZATIONS	DEATHS	TOTAL
Falls	523,043	62,334	9,718	595,095
Struck By/Against	271,713	7,791	378	279,882
Motor Vehicle-Traffic	218,936	56,864	16,402	292,202
Assault	148,471	15,341	5,813	169,625
Other	108,467	27,536	19,252	155,255
Unknown	94,165	105,282	0	199,447

Figure 1.1: Estimated Average Annual Numbers of Traumatic Brain Injury-Related causes in USA, 2002-2006 [1].

1.2 Reading Guide

The dissertation is split into five chapters, a short description is presented below.

Chapter 1 - Introduction: in this chapter, a short introduction is presented, as well as a summary of the content present in each chapter.

Chapter 2 - State-of-the-art: This chapter contains an overview of the human head, broken down into its most relevant components, reviews the types of TBI, and the history of FEHMs.

Chapter 3 - Methodology: this chapter presents the process of constructing the new model and its validation.

Chapter 4 - Simulation and results: the simulation results are presented and analysed in this chapter.

Chapter 5 - Conclusions and future works: At last, this chapter presents the discussion of the results obtained along with the present work and possible ways to improve them in future works.

Chapter 2

State-of-the-art

This chapter reviews the literature on the human head and its components. It also examines the history of finite element head models.

2.1 Anatomy of the head

The head is the most important part of the human body since it contains the brain that controls all body movement and 4 of the 5 human senses. Due to its importance, the human head is classified as the most vulnerable part of the human body. Therefore, head injuries are a very important health problem. To better understand the mechanisms of head injuries, many investigations have been conducted using cadaver heads, animal heads, and physical head models. These experiments, together with the advance in computational technology, led to the development of numerical head models.

With this state of the art, different parts of the human head will be described and the identification of their existing injuries. Finite element head models will also be reviewed.

2.1.1 Skull

The human skull is a very important part of the human body since it forms a structure to support the head and the facial structures as well as forms a cavity where the brain lies. The skull has a total of 22 bones, 14 facial bones, and 8 cranial bones. The cranial bones consist of unpaired frontal, occipital, ethmoid, and sphenoid bones as well as paired parietal and temporal bones [2] while the facial bones are formed by the paired nasal bones, palatine bones, lacrimal bones, zygomatic bones, maxillae, and inferior nasal conchae and the unpaired vomer as can be seen figure in 2.1 [4; 5].

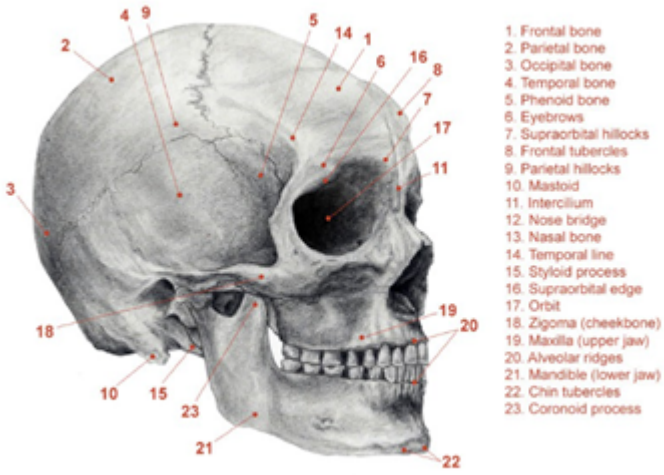

Figure 2.1: Composition of the human skull [5].

The cranial bones of the skull are attached by visible sutures, these sutures are rigid immovable connections holding bones tightly to one another allowing the bones to move during birth and the growth process. Four different cranial sutures, that articulate several cranial bones: Sagittal suture, Coronal suture, Squamous suture and Lambdoid suture as shown in figure 2.2 [6].

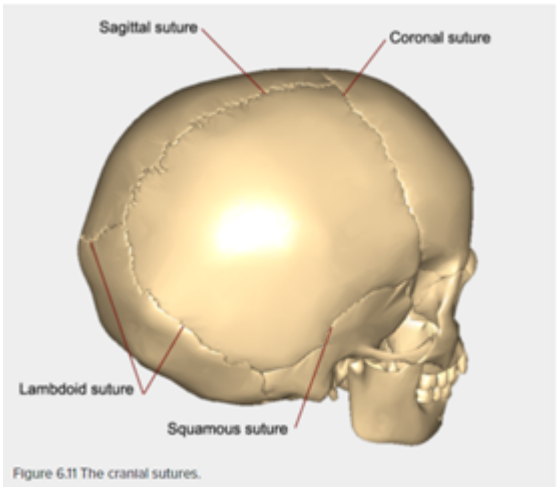

Figure 2.2: All visible sutures of the human skull [7].

2.1.2 Meninges

Meninges are three tissue membranes primarily known as coverings of the brain. They consist of the dura mater, arachnoid, and pia mater as we can see in Figure 2.3. The externally located dura mater consists of tough fibrous connective tissue, this mater attaches at the margin of the foramen Magnum to the occipital bone and forms the inner surface of the second and third cervical vertebrae. The arachnoid is a thin membrane

located between the dura and the pia. The space between the pia and arachnoid, the subarachnoid space, is filled with cerebrospinal fluid (CSF). The arachnoid bridges the cerebral sulci and extends from the posterior surface of the medulla to the cerebellum and below the neural end of the spinal cord. The pia adheres to the central nervous system and is continuous with the perineurium of cranial and spinal nerves. It attaches to the blood vessels entering, leaving the central nervous system, and fusing with the dura [8].

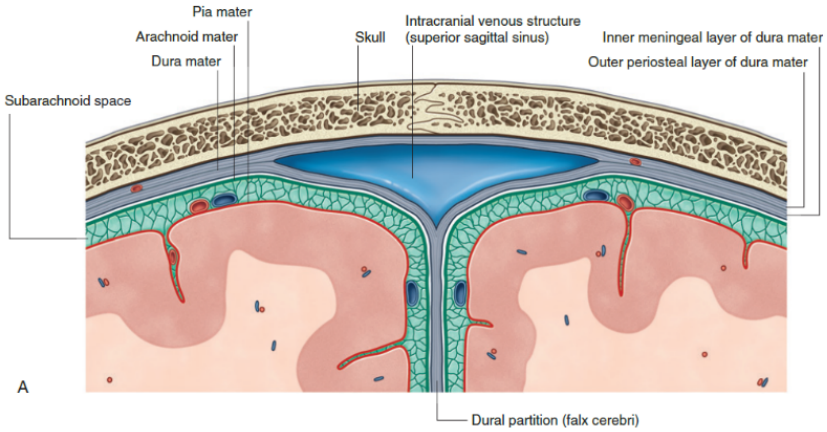

Figure 2.3: Distinction of the Meninges [2].

The primary function attributed to meninges and CSF is to protect the central nervous system (CNS). This is mainly because meninges provide a tight anchoring of the CNS to the surrounding bones able to prevent side-to-side movement and provide stability. Besides covering the brain, recent studies on the meningeal function and its ultrastructure have revealed that meninges largely penetrate inside the neural tissue, having a crucial role in the physiological and pathological events of the CNS throughout life. Meninges have been present since the early embryonic stages of cortical development and appear necessary for normal corticogenesis and brain structure formations [9].

2.1.3 Brain

The human brain weighs on average 1.60kg in men and 1.45kg in women. Containing approximately 1 trillion cells and 100 billion neurons, it constitutes about one-third of the human head mass while receiving roughly 20% cardiac output [9]. The brain is encapsulated by the cranium and bathed in cerebrospinal fluid. Because the density of the brain and cerebrospinal fluid is very similar, the brain neither sinks nor floats in the cerebrospinal fluid [2]. The brain consists of both grey and white matter, unfortunately, due to a lack of consistent data in the literature, it cannot be stated which of the previous is stiffer than the other [3]. The human brain can be divided into three distinct parts, namely the cerebrum, the cerebellum, and the brainstem [10] as shown in Figure 2.4.

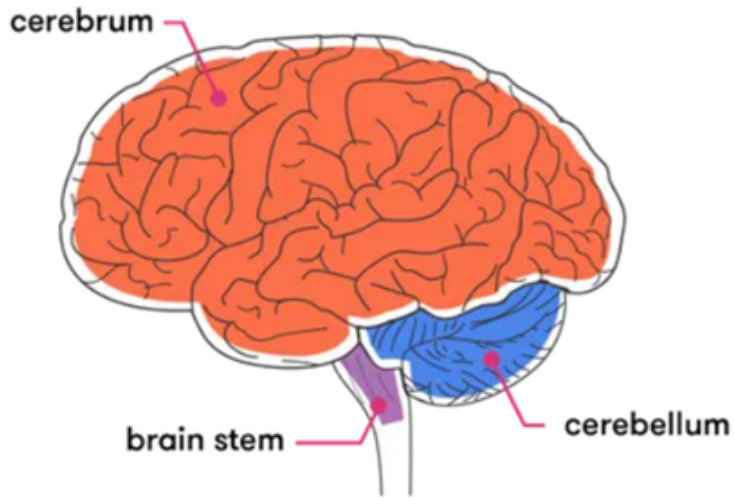

Figure 2.4: Distinct parts composing the brain [11].

Cerebrum

The cerebrum is the most dominant part of the brain. Two different types of matter compose the cerebrum, gray and white matter. The gray matter is the outer layer of the cerebrum, also named the cerebral cortex [12; 13]. This thin layer has a rough appearance due to the presence of rounded bulges and grooves, which are named gyri and sulci, respectively. While the white matter is the inner layer [12]. The cerebrum can also be separated into two distinct halves, a right and left cerebral hemisphere by the main and deepest groove named, the longitudinal fissure [13] as figure 2.6 shows. The cerebral hemispheres are conventionally divided into several lobes by gyri and sulci. The most common division as shown in figure 2.5 consists of four separate lobes: frontal, parietal, temporal, and occipital [11]. The names of the lobes are partly related to the overlying bones of the skull. For example, the frontal lobe is approximately beneath the frontal bone, and likewise, the occipital lobe is under the occipital bones [12].

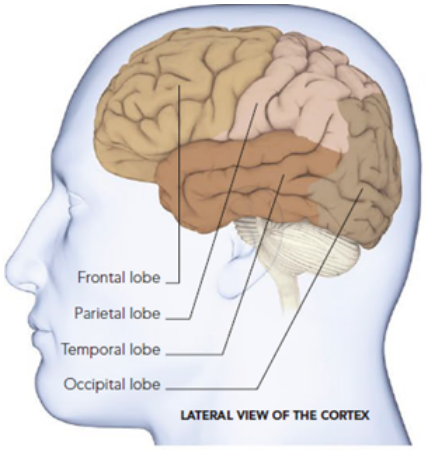

Figure 2.5: Division of the brain in four separate lobes, and their respective position [8].

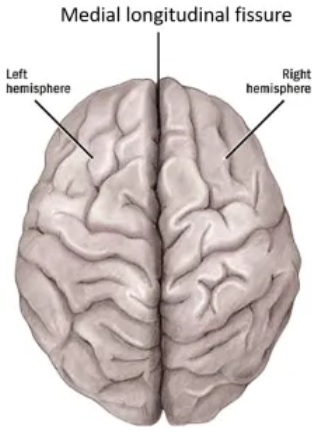

Figure 2.6: Visualization of both hemispheres divided by the Medial longitudinal fissure [12].

Frontal Lobe

The frontal lobes embody the largest region in the cerebrum, representing about 30% of the cortical surface [14]. It is separated from the parietal lobe by a space called the central sulcus, and from the temporal lobe by the lateral sulcus [15]. The frontal lobe can be divided into two main devoted areas of functionality, the posterior areas are more dedicated to motor functions while the anterior areas are dedicated to non-motor functions [8]. Additionally, the left and right frontal lobes are differentiated: the left frontal lobes are more specialized for language-related functions, and the right frontal region is dominant in social cognition and emotion [14].

Parietal lobe

The parietal lobes occupy approximately 25% of the human brain [16]. It is separated from the frontal lobe by the central sulcus, and the occipital lobe by the parieto-occipital sulcus [11], but no clear landmarks enable precise differentiation from temporal lobes [11; 12; 16]. The parietal lobes are responsible for the integration of sensory information, including perception, decision-making, numerical cognition, speech comprehension, and spatial awareness [15; 17]. Besides all of the perceptual processes above, studies held in the early 2000s have shown that the parietal cortex plays an important role in motor control [18]. One of its roles is to integrate sensory and motor signals to accomplish sensorimotor transformations necessary for motor planning and sensory guidance of movements [18].

Temporal lobe

The temporal lobes are separated from the frontal lobe by the lateral sulcus, but such as the parietal cortex, is a poorly defined region without discrete landmarks to separate them from the occipital lobes [11]. The most important function of this cerebrum's region is related to forming and processing memory [11; 15]. Besides that, there are some areas associated with intricate functions, including olfaction, categorization, and association of visual stimuli, face recognition, and emotional perception [11].

Occipital lobe

The occipital lobe, occupying the posterior pole of the brain, constitutes approximately 10% of the brain [19]. The visual cortex, located in this lobe, is the major visual processing center in the brain. It receives visual information from the eyes, that is relayed to several secondary visual processing areas, which interpret depth, distance, location, and the identity of seen objects [15]. Besides that, the visual cortex can access the memory for past visual experiences, since it is directly connected to the temporal lobe [19].

Cerebellum

The cerebellum (from the Latin meaning "little brain") represents about 10% of the mass of the brain and its located at the back of the cerebrum as shown in figure 2.3 [13]. It is very similar to the cerebrum, both in structure and consistency as can be seen in figure 2.7. Structurally, it resembles the wrinkled appearance of the cerebrum, but its grooves and bulges are finer and organized into more regular patterns [12; 13]. In terms of consistency, it is composed of gray matter on the surface and white matter on the inside [8]. The cerebellum's main functions are to coordinate body movements through integrated control of muscles, including balance, posture, and equilibrium [12]. It is largely responsible for comparing information from the cerebrum with sensory feedback from the periphery through the spinal cord [13]. For example, If the primary motor cortex of the frontal lobe sends a command down to the spinal cord to initiate walking, a copy of the instruction is sent to the cerebellum. Sensory feedback from the muscles and joints, proprioceptive information about the movements of walking, and sensations of balance are sent to the cerebellum through the inferior olive and the cerebellum compares them. If walking is not coordinated, perhaps because the ground is uneven or a strong wind

is blowing, then the cerebellum sends out a corrective command to compensate for the difference between the original cortical command and the sensory feedback. The output of the cerebellum is into the midbrain, which then sends a descending input to the spinal cord to correct the messages going to skeletal muscles [13].

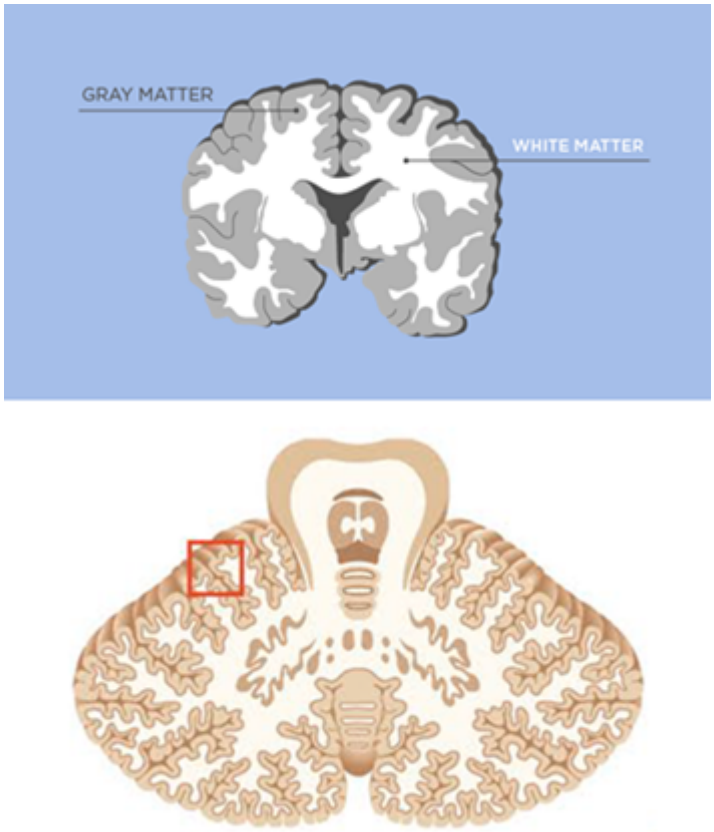

Figure 2.7: Similar appearance between the cerebrum and the cerebellum – adapted from [8; 19].

Brainstem

The brainstem is the lower extension of the brain, located in front of the cerebellum and connected to the spinal cord. In Figure 2.8 It is possible to see the three structures that compose the brainstem: the midbrain, pons, and medulla oblongata [10]. The brainstem's main purpose is dedicated to low-order mental activities, such as the subconscious or autonomic control mechanisms, of which we are usually unaware [12]. The midbrain coordinates sensory representations of the visual, auditory, and somatosensory perceptual spaces [13]. The pons and the medulla oblongata house groups of nerve-cell bodies that are centers for respiratory (breathing), cardiac (heartbeat), and vasomotor (blood pressure) monitoring and control [12; 13].

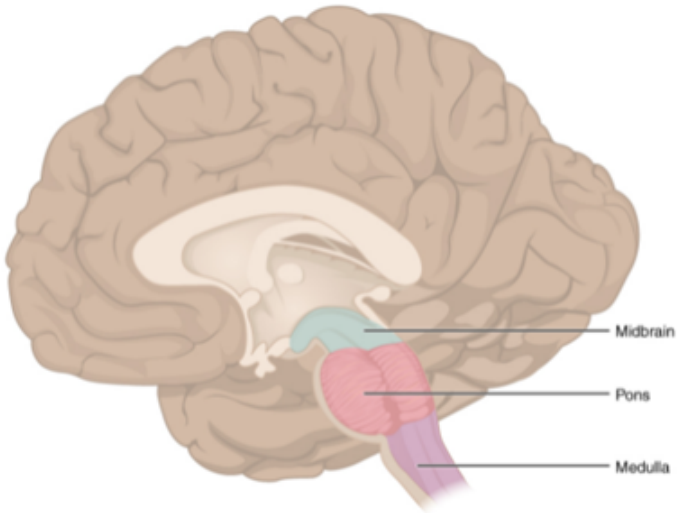

Figure 2.8: Brainstem composition [10].

Human brain properties

Brain tissue is one of the most complex tissues in the human body [20]. And is softer than any other tissue in the human body, figure 2.9 highlights the stiffnesses of various organs in our body [20]. With a shear modulus on the order of one kilopascal [21], brain tissue is ultrasoft. The low stiffness makes it very complicated to use the traditional mechanical test setups, due to the force sensors reaching their sensitivity limit [20]. As a result, early studies on the stiffness of brain tissue yielded significantly higher values than more recent studies [22]. Brain tissue is highly fragile, making it difficult to control tissue damage during biomechanical testing, especially when applying large deformations. In addition, the effect of adhesion enhances the risk of damaging specimens during preparation and handling [20]. To combat these problems, new in vivo non-invasive techniques based on magnetic resonance elastography have now been developed to investigate biological soft tissue [23].

Unlike other soft tissues, the brain is not only ultrasoft but also has an exceptionally high water content, 0.83g/ml in gray matter and 0.71 g/ml in white matter [24], making it nearly incompressible [21; 25].

To understand how an external mechanical load can create injuries in the case of brain trauma, it is essential to characterize the mechanical behavior of the brain. The detailed mechanical parameters of brain tissue are needed to deduce brain material constitutive laws that can then be implemented in finite element models of the head [23].

The most common way to describe the mechanical behavior of the brain, it's by assuming it as a non-linear viscoelastic solid material [21]. More recently, in vitro results completed with dynamic frequency sweep experiments made it possible to observe brain properties such as non-linear behavior, anisotropy, and strain rate dependence [22]. In terms of age dependence, Thibault and Margulies [25] showed that storage, loss, and complex shear moduli seem to increase with age. It was concluded that the shear modulus of young brain tissue is independent of strain-level whereas the shear modulus of adult brain tissue

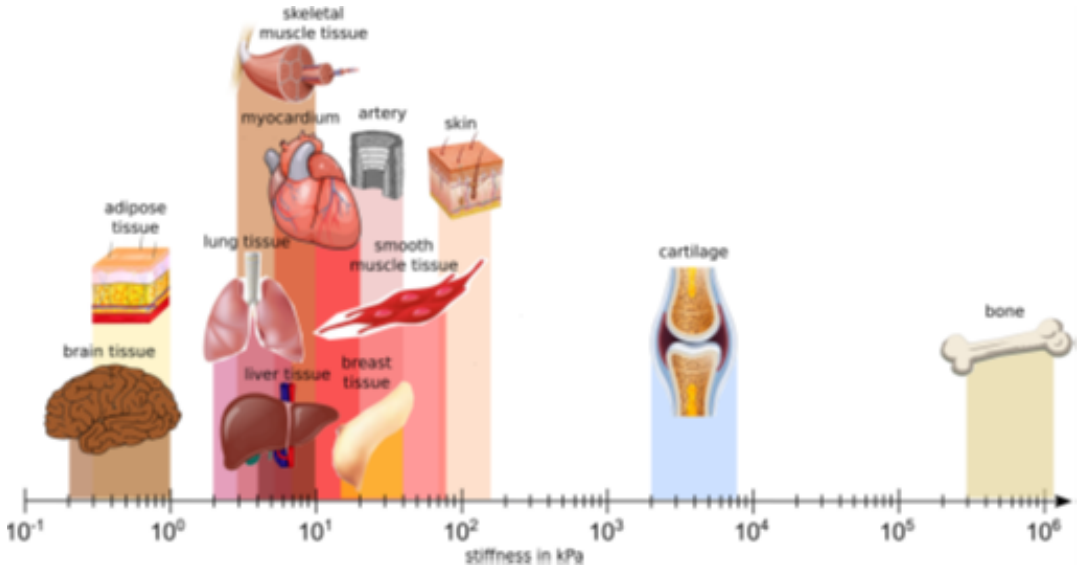

Figure 2.9: Stiffness of various organs in human body [20].

decreases when strain increases [23]. On the other hand, several studies have revealed that the brain tends to soften as it ages, with annual changes in stiffness between 0.3-1% [26]. In summary, brain tissue is a very soft, strain-rate sensitive, non-linearly viscoelastic solid material, with a very low linear viscoelastic strain limit (0.1-0.3%) and a moderate strain failure limit (25-100% depending on the loading type) [3].

2.2 Traumatic brain injuries

Traumatic brain injuries (TBIs) can affect people of all ages and are a major cause of death and disability, with an incidence of 10 million people worldwide [27]. There are various methods to categorize TBI. They can be categorized based on occurrence, location, or severity as shown in figure 2.10 [2]. Based on their occurrence, TBI can be categorized as a primary or secondary injury. Primary injury is the direct result of the initial trauma, such as cortical surface contusions, hematomas, and lacerations. Secondary brain injuries are associated with the evolution of the initial injury, for example, altered cerebral blood flow, hypoxia, and infection, among others [2]. Another common classification is simply dividing, penetration (in which an object breaches the skull and dura, with direct damage to the brain) versus non-penetration injuries (in which the skull and dura remain intact) [27]. The most common way to classify it is by location, which divides them into focal (localized) injuries and diffuse (widespread over the area) injuries [2].

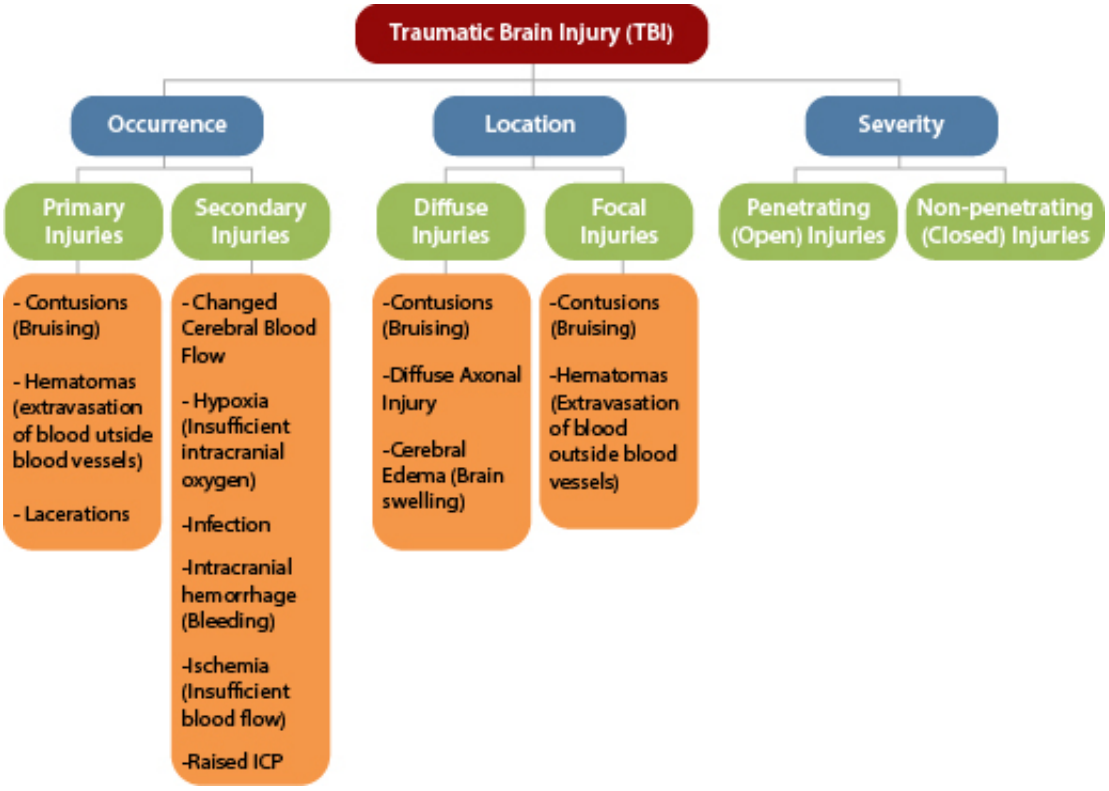

Figure 2.10: Classifications of traumatic brain injury (TBI) [2].

2.2.1 Focal injuries

Most focal brain injuries occur due to direct contact with bone fragments from skull fractures, or to relative motion between different parts of the skull and the brain. Such relative motion may be due to linear or rotational acceleration of the skull [28]. These injuries are typically associated with blows to the head that leads to cerebral contusions and hematomas [29].

Contusion

A contusion is the most frequent focal injury and can be divided into coup and contrecoup contusions. Coup contusion appears at the site of impact while contrecoup appears at the opposite side of the head [30]. The term contusion is used when the pia is not breached, otherwise, we should call them lacerations [31]. Most severe contusions happen in the crests of gyri, due to their proximity to the skull and where the surface of the brain meets bony protuberances in the skull. Thus, they occur particularly under the surfaces of the frontal lobes, and the under surfaces of the temporal lobes. [28; 31].

Hematoma

Intracerebral hematomas (ICH) are a well-defined cluster of blood created by a ruptured blood vessel, they are usually associated with contusions and therefore occur particularly in the frontal and the temporal lobes [31]. Epidural hematoma (EDH) is caused by trauma or a skull fracture that causes ruptures of the underlying meningeal vessels, where the dura is stripped away from the skull, producing a potential space into which haemorrhage occurs [30; 32]. Subdural hematoma (SDH) is caused by a rupture of an artery or bridging veins, making them one of the most fatal brain injuries. This injury is directly related to rotational effects on the brain [30]. figure 2.11 shows the different Hematomas.

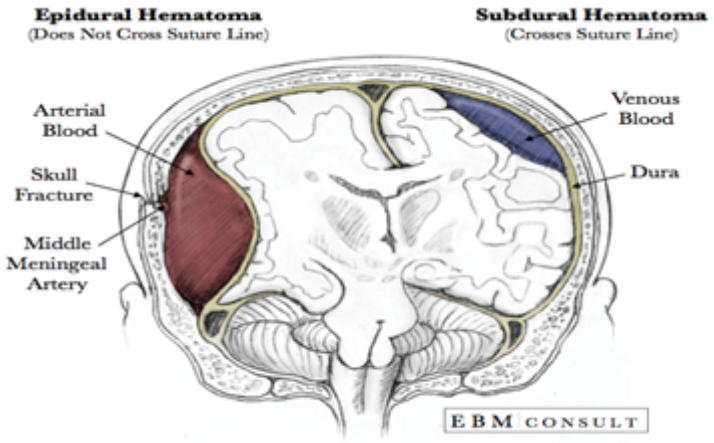

Figure 2.11: Difference between Epidural and Subdural Hematomas [33].

2.2.2 Diffuse injuries

The concept of diffuse brain injuries was introduced due to the absence of focal lesions observed on medical images [32]. These injuries may occur without impact forces directly applied to the head, as they are formed by inertial forces. These inertial forces are a result of rapid head rotational motions, which deforms the White matter [29]. Diffuse brain injuries consist of concussions, swelling of the brain, and diffuse axonal injury (DAI) [28].

Diffuse axonal injury

DAI is associated with widespread disruption of axons in the cerebral hemispheres, midbrain, and brainstem. DAI involves loss of consciousness lasting at least 24 hours and possibly weeks [28]. In mild to low DAI, there is a remarkable absence of macroscopic pathology and the brain seems normal. Only on the microscopic examination of the brain tissue, is it possible to observe the disconnected axons. High severity DAI is one of the deadliest brain injuries recorded [29].

Concussion

A concussion is the most common head injury, which can be caused by a blow to the head, and violently shaking of the head and upper body [30; 34]. A mild concussion may include disorientation and confusion, with a moderate concussion leading to loss of consciousness for up to 24 hours. Besides that, low to moderate concussions tend to have no life-risking treatment and have a good recovery rate [28].

2.2.3 Head injury criteria

Current standards used usually by sports and automotive industries for head injury prediction and protection are the Gadd Severity Index (GSI) [33] and the Head Injury Criterion (HIC) [35], although there are controversies about these indices [36] since they depend solely on the translational acceleration of the head, disregarding the rotational acceleration [34]. Furthermore, these indices, which are based on Wayne State Tolerance Curve (WSTC) data, are derived from frontal impacts only [37]. Later studies [38; 39] proposed another injury criterion entitled the Head Impact Power (HIP) which associates both translational and rotational head accelerations. Table 2.1 will show a summary of the proposed limits in the literature for brain injury.

Table 2.1: Proposed limits in the literature for brain injury - adapted from [2].

Parameter	Location	Thresholds	Type of injury	Reference
Intracranial pressure (kPa)		>235	Brain Injury	Ward et al. (1980) [40]
		>300	Mild TBI	Newman et al. (2000) [39]
	Coup	66 – 114	Brain Injury	Zhang et al. (2004) [34]
	Contrecoup	-101 – -51	Brain Injury	Zhang et al. (2004) [34]
Shear stress (kPa)		11 – 16.5	Severe Injury	Kang et al. (1997) [41]
		8 – 16	Severe Injury (mild DAI)	Anderson et al. (2004) [42]
	Midbrain	6.2 – 10.6	Brain Injury	Zhang et al. (2004) [34]
	Midbrain	>6.6	Brain Injury	Zhang et al. (2004) [34]
	Upper brainstem	>7.8	Mild TBI	Zhang et al. (2004) [34]
	Thalamus	3.3 – 5.7	Brain Injury	Zhang et al. (2004) [34]
Von Mises stress (kPa)		>11	Brain Injury	Zhou et al. (1996)[43]
		>15	Brain Injury	Kang et al. (1997) [41]
		>7	Contusion	Miller et al. (1998) [44]
		>27	Brain Injury	Anderson (2000) [45]
		>20	Mild TBI	Newman et al. (200) [39]
		15 – 20	Concussion	Willinger et al. (2000) [46]
		>39	Severe neurological	Willinger and Baumgartner (2001) [47]
		>38	Severe neurological	Willinger and Baumgartner (2003) [48]
		>26	Axonal damage	Deck and Willinger (2008) [49]
Translational acceleration (g)		>76	Closed head injury (for 20ms duration)	McElhaney et al. (1973) [50]
		>220	Injury (for 2ms duration)	Ono et al. (1980) [51]
		>90	Injury (for 9ms duration)	Ono et al. (1980) [51]
		73 – 133	Injury	Zhang et al. (2004) [34]
Rotational acceleration ($rads^{-2}$)		>4500	Gliding contusion	Lowenhielm (1975) [52]
		>16000	Injury	Princemaille et al. (1989) [53]
		>16000	Moderate to severe DAI	Margulies and Thibault (1992) [54]
		4457 – 10251	Injury	Zhang et al. (2004) [34]
		2793 – 5615	Non-injury	Zhang et al. (2004) [34]

2.3 Finite element head model (FEHM)

For several decades, animals, cadavers, and volunteer living subjects have been used extensively in experimental tests to investigate head injury problems. Despite the valuable information provided by the experimental data, due to legal and ethical reasons, as well as the risk of injury, obtaining data from living human subjects is now impossible [2; 3]. Thereafter, human simulacra or dummies were introduced using information retrieved

from animal testing and cadaver research. However, damaged dummy parts after experiments require replacement which required costs [2]. Therefore, finite element head models (FEHM) were developed.

2.3.1 History of FEHM

The first attempt to model the behavior of the human head response through FEM was made by Hardy and Marcal [55], who built a two-dimensional (2D) FEHM, consisting of only the skull that was later improved by Shugar [56] by adding an elastic, fluid-filled brain that is attached to the skull. Due to the lack of computational resources in the 1970s, 2D plane deformation models were the only means to simulate impacted head deformations. The first three-dimensional (3D) FEHMs were highly simplistic, using regular geometries such as spheres or ellipses [57; 58]. For example, Chan [59] modeled the human head as a spherical shell and a prolate ellipsoid, while Khalil and Hubbard [58] used an ellipsoid shell for the skull. These simplified models considered the anatomical and material properties of only one of the two main structures, the skull or the brain. A 3D model that represented the basic anatomy of both structures was developed by Hosey [60] in 1981. His model was considered the most comprehensive head and neck model back then [61], besides including the anatomy of the head, brain, and neck, Hosey took the inertial and material properties of the head and neck into account. A representation of the model can be seen in figure 2.12. Even though these FEHMs are considered unrealistic today, they represented a first step in the theoretical analysis of the biomechanics of head injuries. Only in the 1990s, due to the advance in computing capability, making it was possible to develop a more realistic and comprehensive 3D FEHM based on the actual geometry of the human head.

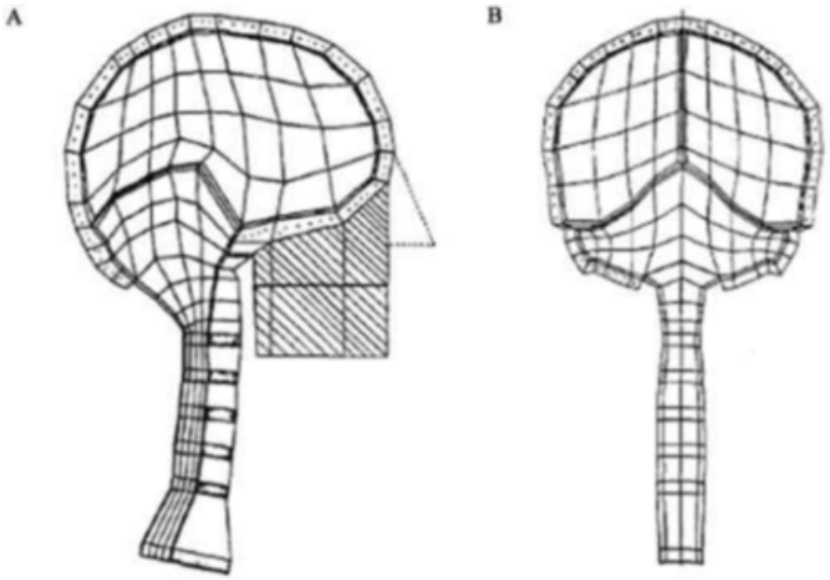

Figure 2.12: FEHM developed by Hosey [60]. (A) Sagittal cross section; (B) Coronal cross section [2].

The first realistic model developed was created by Ruan et al. [62], the model consisted of the detailed anatomy of the skull and brain shown in figure 2.13. This FEHM was the first version of the Wayne State University Brain Injury Model (WSUHIM). The skull, brain, and CSF were developed with eight-node hexahedron elements, while the scalp, dura mater, and brain scythe were modeled with four-node shell elements. The same model was further enhanced by Zhou et al. [63] in 1995 which differentiated grey and white matter. The model was refined by Zhang et al. [64] in 2001 by introducing a sliding interface between the skull and the brain, achieving more precise results.

Ultimately, King et al. [65] completely revised and improved the previous version of WSUHIM, this time including the scalp, a three-layered skull, dura, falx cerebri, tentorium, pia matter, CSF hemispheres, cerebrum, cerebellum, ventricles, brainstem, and the facial bones. The fully revised model simulated most of the essential anatomical features of a 50th percentile male head. This latest revised version of WSUHIM contained 314500 elements.

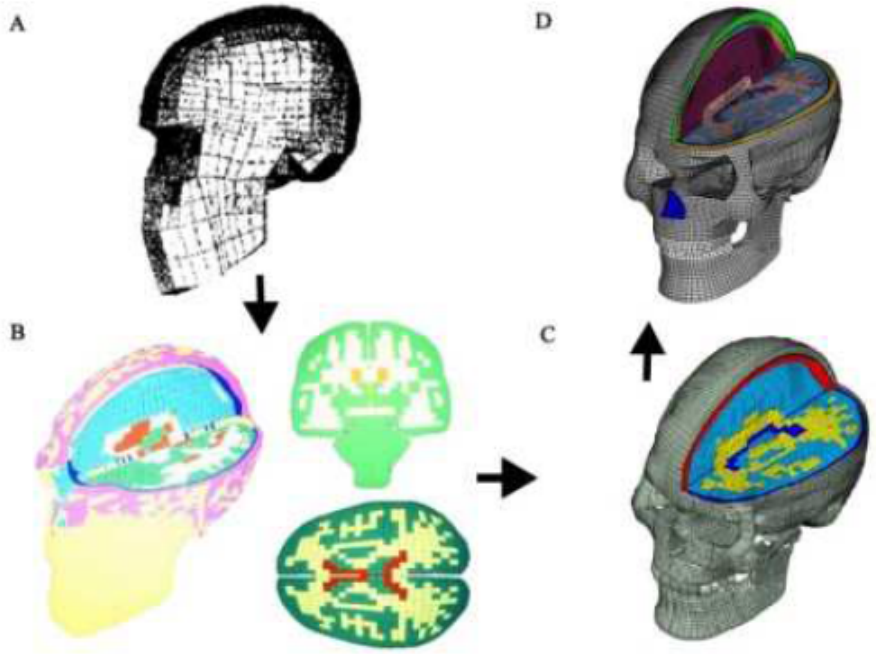

Figure 2.13: FEHM developed by Hosey [60]. (A) Sagittal cross section; (B) Coronal cross section [2].

Another FEHM that is worth mentioning is the Strasbourg University Finite Element Head Model (SUFEHM), which was developed by researchers Kand and Willinger in 1997 [66] including almost all mechanically relevant parts of the head, e.g. the scalp, skull, brain, CSF, tentorium, and falx as we can see in figure 2.14. The group introduced a Lagrangian approach to model the CSF and an elastic-brittle constitutive law for the skull-brain interface. This model consists of 13208 brick elements and 2813 shell elements and makes it possible to calculate internal brain pressure [67].

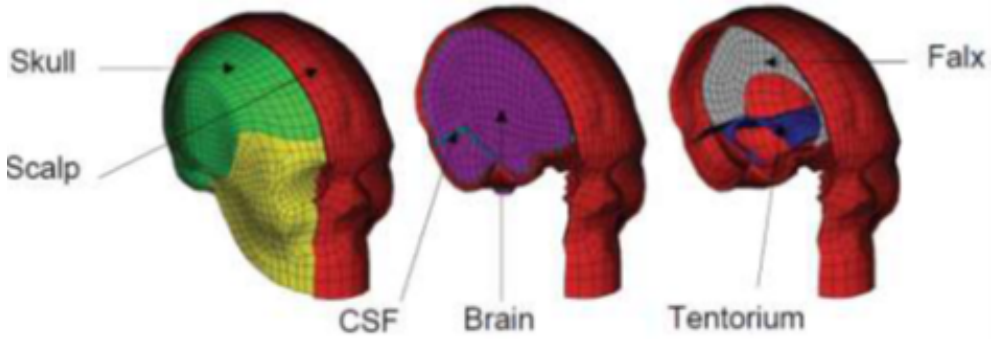

Figure 2.14: The Strasbourg University Finite Element Head Model (SUFEHM). Adapted from [68].

In 2002, Kleiven and Hardy [69] built a detailed model of an adult FEHM, known as Kungliga Tekniska Högskolan (KTH) FEHM illustrated in figure 2.15, the model included scalp, skull, brain, meninges, CSF, eleven pairs of bridge veins and simplified neck. The KTH FEHM consisted of 18400 elements and was modeled with isotropic, homogeneous, nonlinear, and viscoelastic material properties. In their model, the inner and outer surfaces of the skull are scaled independently, making it possible to adjust the width, length, height, and thickness of the skull. The brain material properties were modeled using a hyperelastic and viscoelastic constitutive law.

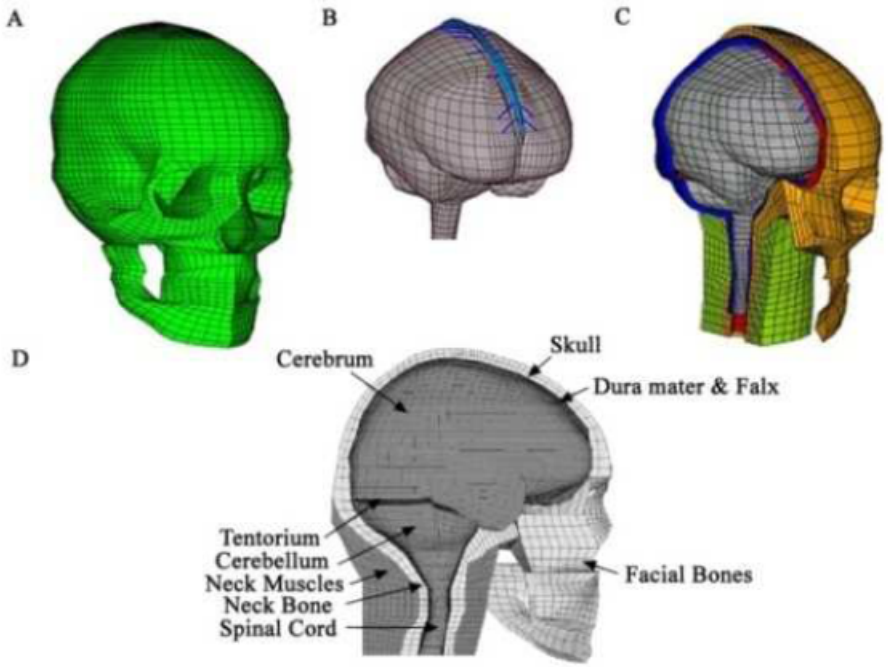

Figure 2.15: Kungliga Tekniska Högskolan (KTH) FEHM. (A) skull; (B) brain with bridging veins; (C) cut view of the head and neck model; (D) anatomical structures [2].

Horgan and Gilchrist [70] 2003 constructed the University College Dublin Brain Trauma Model (UCDBTM) to simulate the transient occurrences of simple pedestrian accidents. Their skull-brain complex includes a scalp, a three-layered skull, dura mater, CSF, pia mater, cerebral scythe, tentorium, cerebral hemispheres, cerebellum, and brainstem as shown in figure 2.16. Two models were created. In the first one, the scalp was modeled using Shell elements, cortical and trabecular bone with brick elements, the dura with membrane elements, CSF with brick elements, pia with membrane elements, falx, and tentorium with Shell elements, and the cerebrum, cerebellum, and brainstem with brick elements. The difference in the second model was the skull was constructed using a composite Shell element, and the scalp was modeled with brick elements. Note that a linearly viscoelastic material model combined with a large deformation theory was chosen to model the brain [70]. The models were validated by the experiments of Nahum et al. [71]. Table 2.2 summarises the material properties used for the brain in the history of FEHM.

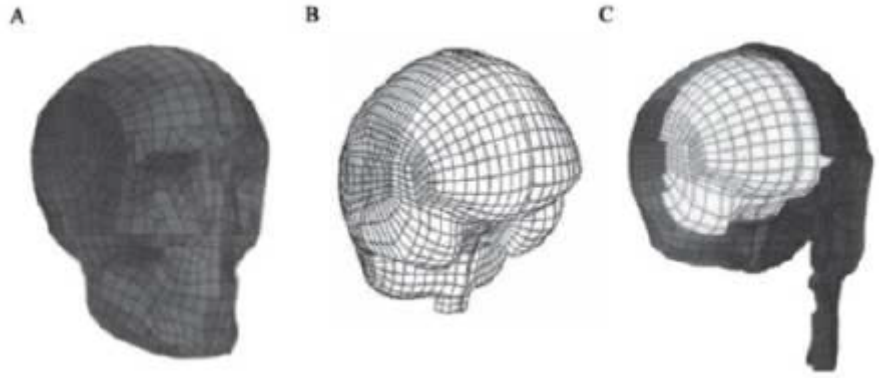

Figure 2.16: The University College Dublin Brain Trauma Model (UCDBTM). (A) the skull; (B) the brain; (C) cut view illustrating the intracranial content [2].

Table 2.2: Material properties used for the brain in the history of FEHM – adapted from [2].

Model Type	E (MPa)	ν	Density, (kg/mm^3)	K (MPa)	Shear Modulus/Viscoelasticity G(t)= $G_\infty + (G_0 - G_\infty)e^{-\beta t}(MPa)$	References
Linear Elastic	8.00E-02	0.49				[72]
Linear Elastic	6.67E-02	0.48				[73]
Linear Elastic	6.75E-01		1.14E-06	5.63E+00		[74]–[75]
Linear Elastic			1.03E-06	2.19E+03		[58]
Linear Elastic		0.4996	1.04E-06	2.19E+03		[76]
Linear Elastic/Viscoelastic	6.75E-01		1.14E-06	2.19E+03	$G_0 = 0.528MPa, G_\infty = 0.168MPa, \beta = 35s^{-1}$	[74], [77], [75], [78], [79]
Viscoelastic			1.00E-06		$G_0 = 0.001036MPa, G_\infty = 0.000185MPa, \beta = 16.5s^{-1}$	[80]
Viscoelastic				1.13E+03	$G_0 = 0.049MPa, G_\infty = 0.0168MPa, \beta = 145s^{-1}$	[46]
Viscoelastic				2.19E+03	$G_0 = 0.033MPa, G_\infty = 0.006MPa, \beta = 700s^{-1}$	[81]
Viscoelastic					$G_0 = 0.010MPa, G_\infty = 0.002MPa, \beta = 80s^{-1}$	[64]
Viscoelastic		0.4996	1.04E-06		$G_0 = 0.043MPa, G_\infty = 0.008MPa, \beta = 500s^{-1}$	[82]
Hyperelastic						[69]
Hyperelastic		0.499981	1.04E-06			[70], [83]

2.3.2 Comparison between different element types

The goal in choosing a particular element type is to find the best balance between simulation accuracy, computational time, convergence rate, and difficulty in generating a mesh for a certain model. The two most common element types used for numerical simulations are hexahedral and tetrahedral. Wang et al [84] conducted some experiments for different mechanical problems, comparing the results between tetrahedral and hexahedral shaped elements. The comparison was made for linear static problems, modal analysis and nonlinear analyses involving large deflections, contact and plasticity. As can be seen in figure 2.17, Wang et al [84] concluded the following:

- Avoid linear tetrahedral elements. They are too stiff, and prone to looking phenomena.
- Quadratic tetrahedral elements are very good, but computationally expensive.
- Linear Hexahedral elements are sensible to the corner angle, making them hard to manipulate in complex geometries.
- Quadratic hexahedral elements are very robust, but computationally expensive.

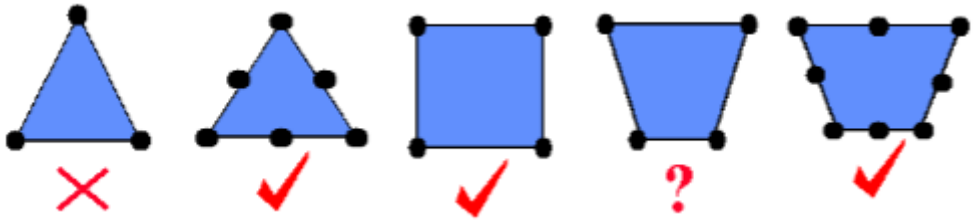

Figure 2.17: Solid elements recommendations. It holds for the two dimensional and also for the three dimensional case - adapted from Wang et al. [84].

2.3.3 Yet Another Head Model (YEAHM)

YEAHM is a finite element head model developed by Fernandes et al. [3] containing a skull, brain, and CSF, was further improved by Migueis [85], Costa [86], and Barbosa [87], adding the bridging veins and hexahedral skull respectively. This model contains several features, for instance, the sulci and gyri are well defined, giving a better representation of the brain geometry. Another characteristic is the type of interaction between parts. Most of the models have shared nodes, which influence the brain's intracranial motion. Supported on this, YEAHM was made considering the relative motion between the brain and the skull.

This model was developed using medical imaging from a 65-year-old male human head, based on magnetic resonances for soft tissues and CT scans for the construction of bony structures. figure 2.18 summarizes the methodology used to create the FE model.

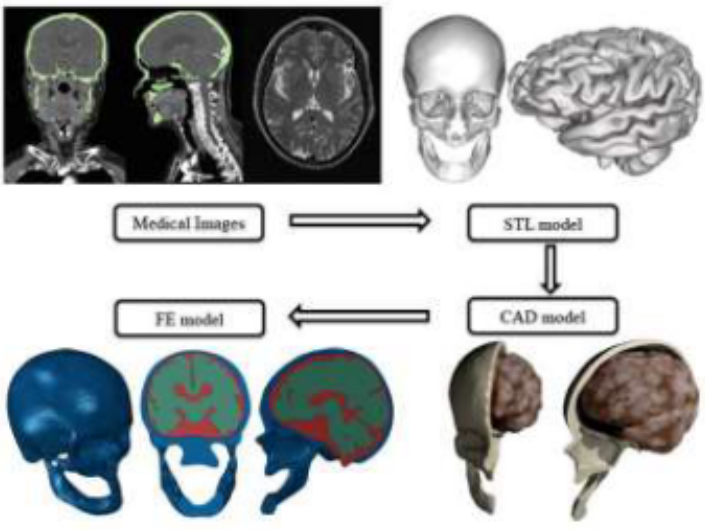

Figure 2.18: Methodology used in YEAHM. Adapted from Fernandes [88].

Components of YEAHM

The head model contains the skull with the distinction between the various type of bones, brain, CSF, and bridging veins (BV) with the superior sagittal sinus (SSS). This base model that served as the basis for this dissertation is a homogeneous model, without any distinction between the grey and White matter, that will be added in this dissertation. figure 2.19 shows the constitution of the base model used in the dissertation, showing the skull (red), CSF (blue), brain (green), and bridging veins (grey).

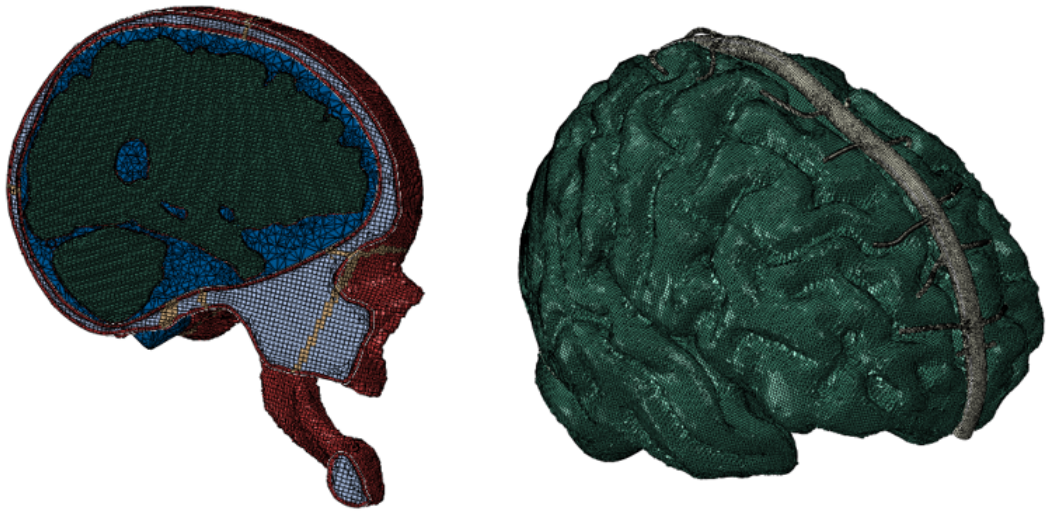

Figure 2.19: Constitution of YEAHM model. Skull (red) with all the sutures (yellow), trabecular bone (white), CSF (blue), brain (green) and the bridging veins (grey).

Material modelling

The model of the material adopted for the brain tissue was a hyper-viscoelastic model. A hyperelastic model was used to describe the non-linear elasticity, combined with a viscoelastic model to describe the time-dependent behaviour. Each hyperelastic model has its strain energy per unit of reference volume W, from which the relationship between strain and stress tensors is derived. The hyperelastic model used for the brain was the Ogden model [89], which has been used in the past by other authors, to describe the non-linear mechanical behaviour of the brain, as well as of other non-linear soft tissues [90; 91; 92]. The Ogden hyperelastic function is given by the equation 2.1:

$$W = \sum_{i=1}^{\mathrm{N}} \frac{2\mu_i}{\alpha_i^2}(\bar{\lambda}_1^{\alpha_i} + \bar{\lambda}_2^{\alpha_i} + \bar{\lambda}_3^{\alpha_i} - 3) + \sum_{i=1}^{\mathrm{N}} \frac{1}{D_i}(J-1)^{2_i} \tag{2.1}$$

Where $\bar{\lambda}_i$ are the deviatoric principal stretches, J is the total volume ratio, N, μ_i, α_i and D_i are material parameters. The bulk modulus and initial shear modulus for the Ogden form are given by equations 2.2 and 2.3, respectively:

$$K_0 = \frac{2}{D_1} \tag{2.2}$$

$$\mu_0 = \sum_{i=1}^{\mathrm{N}} \mu_i \tag{2.3}$$

Therefore, the one-term Ogden hyperleastic function is given by:

$$W = \frac{2\mu_0}{\alpha_i^2}(\bar{\lambda}_1^{\alpha_1} + \bar{\lambda}_2^{\alpha_1} + \bar{\lambda}_3^{\alpha_1} - 3) + \frac{1}{D_i}(J-1)^2 \tag{2.4}$$

The elastic and viscoelastic behaviour of brain tissue can be characterized using Ogden-based non-linear viscoelastic model [93]. The relaxation response was based on a Prony series, and the strain energy function was developed in the form of a convolution integral. Thus, when combining the one-term Ogden hyperelastic model and a Prony series, a hyper-viscoelastic model can be characterized by the following equation 2.5:

$$W = \frac{2}{\alpha_i^2}\int_0^t \left[\mu(t-\tau)\frac{d}{d\tau}(\bar{\lambda}_1^{\alpha_1} + \bar{\lambda}_2^{\alpha_1} + \bar{\lambda}_3^{\alpha_1} - 3)\right] d\tau + \frac{1}{D_i}(J-1)^2 \tag{2.5}$$

Where, the relaxation of the time-dependent shear modulus $\mu(t)$ to describe the viscous response of the tissue is:

$$\mu(t) = \mu_0 \left[1 - \sum_{k=1}^{\mathrm{N}} g_k(1 - e^{-t/\tau_k})\right] \tag{2.6}$$

With μ_0 being the initial shear modulus, τ_k the characteristic relaxation times and g_k the relaxation coefficients.

The parameters for one-term Ogden model and for Prony series used by YEAHM, are based on the ones determined by Rashid et al. [93]. Properties used to model the brain can be seen in table 2.3

Although the mechanical properties of grey and white matter are expected to be different, there is no consistency in data reported in the literature on which brain matter is stiffer than the other [94]. So the brain was assumed to be homogeneous and isotropic.

Table 2.3: Brain modeling properties - adapted from Fernandes [3]

$\rho(kg/m^3)$	$\mu(MPa)$	α_1	$D_1(MPa^{-1})$	g_1	g_2	$\tau_1(s)$	$\tau_2(s)$
1040	0.012	5.0507	0.04	0.5837	0.2387	0.02571	0.0257

The CSF was modelled as a solid using Mooney-Rivlin strain energy potential hyperelastic model with a very low shear modulus. The Mooney-Rivlin strain energy function used is given by:

$$W = C_{10}(\bar{I}_1 - 3) + C_{01}(\bar{I}_2 - 3) + \frac{1}{D_1}(J-1)^2 \tag{2.7}$$

Where W is the strain energy per unit of reference volume, C_{10}, C_{01} and D_1 are material parameters. The bulk modulus and initial shear modulus are given by:

$$K_0 = \frac{2}{D_1} \tag{2.8}$$

$$\mu_0 = 2(C_{10} + C_{01}) \tag{2.9}$$

The values used to model CSF are shown in table 2.4.

Table 2.4: CSF properties - adapted from Fernandes [3]

$\rho(kg/m^3)$	$C_{10}(MPa)$	$C_{01}(MPa)$	$D_1(MPa^{-1})$
1000	0.9	1	0.9

Bridging veins and the SSS were modeled with an elastoplastic law. The properties used can be seen in table 2.5.

Table 2.5: BV/SSS properties - adapted from Costa [86]

E (MPa)	ν	Fracture Strain	Stress Triaxiality	Strain rate (s^{-1})	Displacement at fracture
25.72	0.45	0.31875	0.33	135.86	0.05

The first skull was built using a single isotropic linear elastic material and the properties used are shown in table 2.6.

Table 2.6: Skull properties - Adapted from Fernandes [3]

$\rho(kg/m^3)$	E (MPa)	ν
1800	6000	0.21

Barbosa [87] later improved this geometry. The redesigned skull model now includes two stages to describe its mechanical behaviour: prior to and after cracking. Prior to cracking, a linear elastic material model defines its mechanical behaviour. The chosen values to describe the elastic behaviour for the trabecular bone, cortical bone and cranial sutures can be seen in 2.7.

Table 2.7: New skull properties - adapted from Barbosa [87]

Geometry	E (MPa)	$\rho(kg/m^3)$	ν
Trabecular	1000	1500	0.05
Cortical	20000	1900	0.21
Sutures	15000	2100	0.3

To define the behaviour of bone tissue after cracking, three parameters were defined: a post-failure stress-strain relation, a shear retention model and a brittle failure criterion. Figure 2.20 shows the values used for cortical and sutures tissues, regarding the post-failure stress-strain relation.

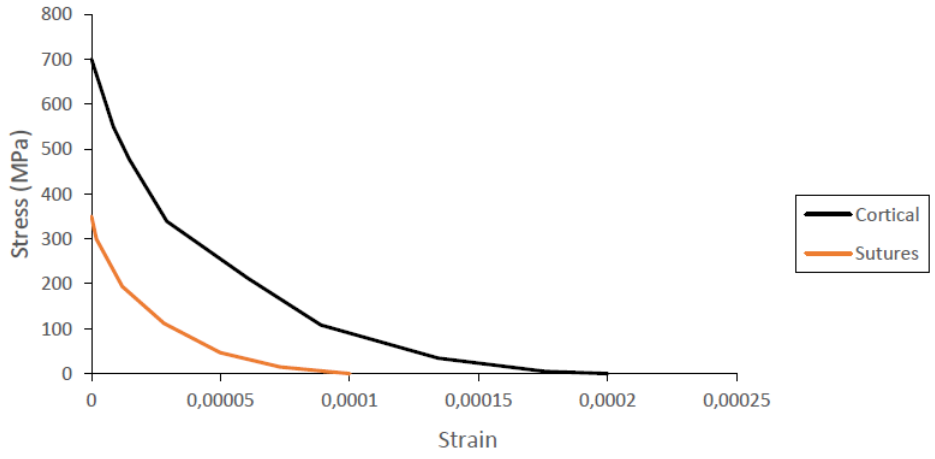

Figure 2.20: Post-failure stress-strain curve for both cortical and sutures tissues - adapted from Barbosa [87].

Regarding the shear retention model, figure 2.21 shows the relation employed for both cortical and sutures tissues.

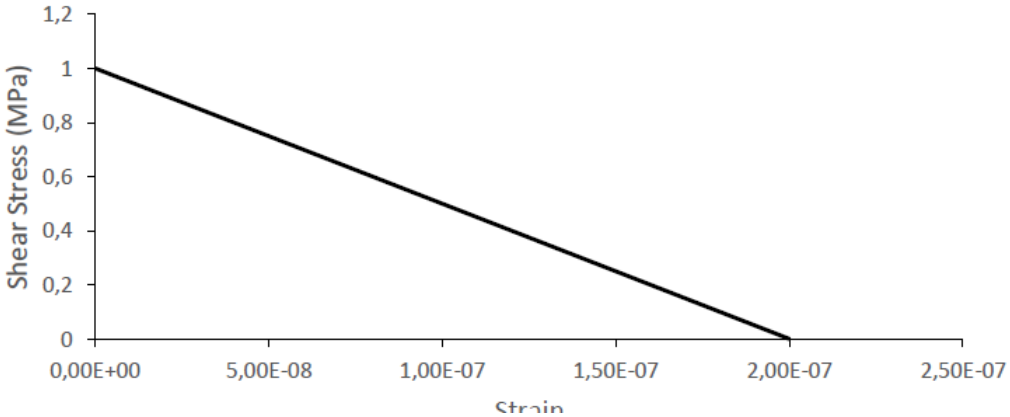

Figure 2.21: Shear retention model values for both cortical and sutures tissues - adapted from Barbosa [87].

Lastly, Barbosa [87] defined a direct cracking failure strain of 0.0006 for the cortical bone, and 0.0004 for the cranial sutures.

Chapter 3

Methodology

In this chapter the methodology used to create the brain model is presented and the methods used to validate it.

3.1 Geometrical modelling of the brain

3.1.1 Model 1

As previously mentioned, this work will use the latest YEAHM model, developed by Fernandes et al. [3] and improved over the years by former students from the Mechanical Engineering Department of the University of Aveiro. The focus of this work it's to create a hexahedral mesh for the brain and subdivide it from white and grey matter. Firstly, because of the absence of good tools to edit complex meshes in Abaqus, the STL file (figure 3.1) of the brain model was imported to Hypermesh (Altair, USA). This software is a finite element pre-processor with several tools for editing complex meshes, with great mesh generator algorithms.

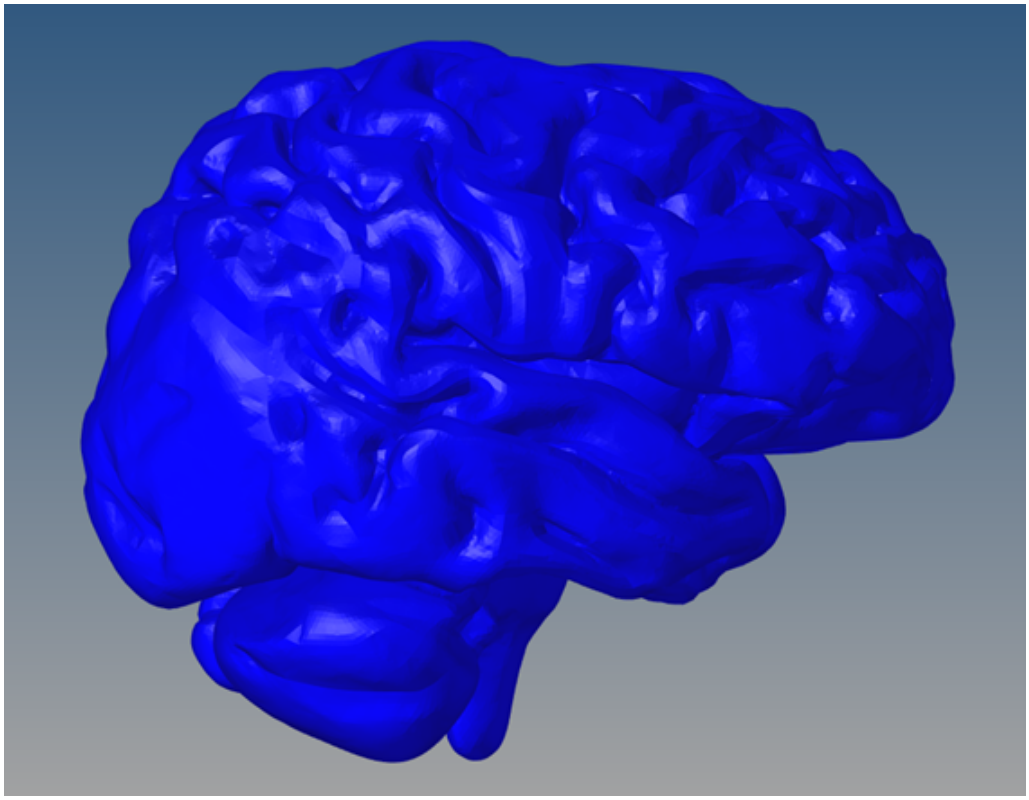

Figure 3.1: STL file of the brain model imported to hypermesh.

After that, a component with hexahedral elements was created using a 'Shrink Wrap Mesh' algorithm, as seen in figure 3.2. The parameters were chosen to ensure acceptable elements aspect ratios were given by an element size of 1 mm and a minimum Jacobian of 0.3.

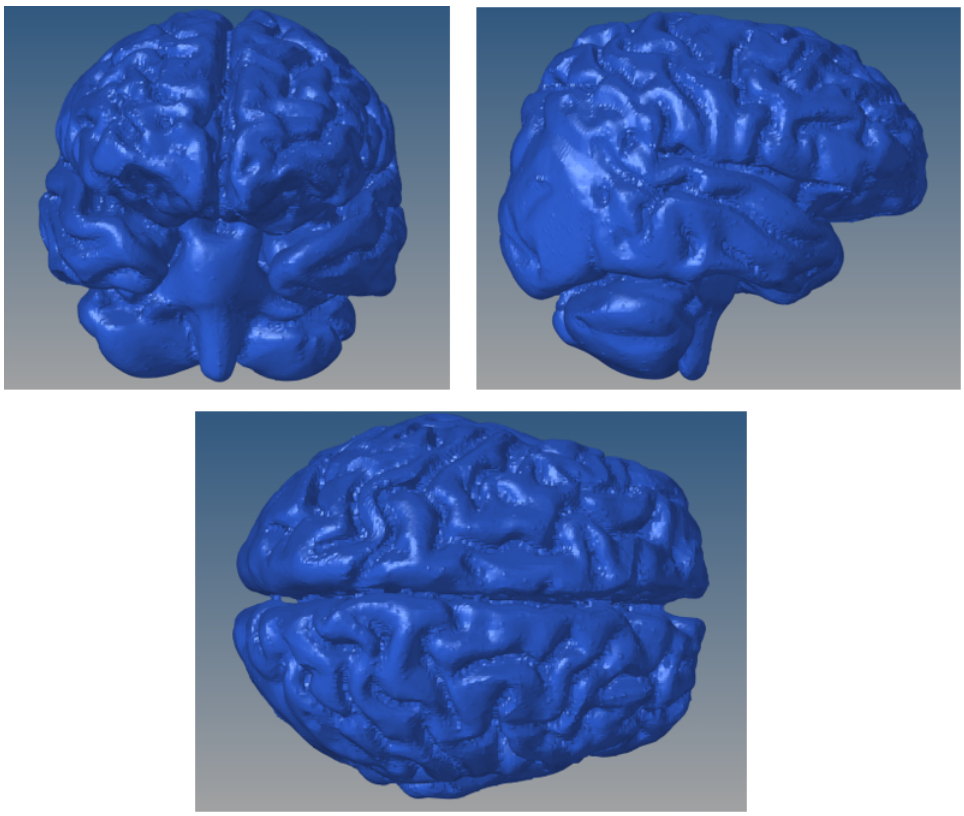

Figure 3.2: Front, side and top view of the brain model.

Although the quality of the mesh was good and resembled the geometry model, it occurred that the two brain hemispheres were connected in several parts instead of only being connected in the original place (Corpus Callosum), compromising the brain's structural rigidity. The same thing happened with both hemispheres becoming connected with the cerebellum. Figures 3.3 and 3.4 shows these problems highlighted.

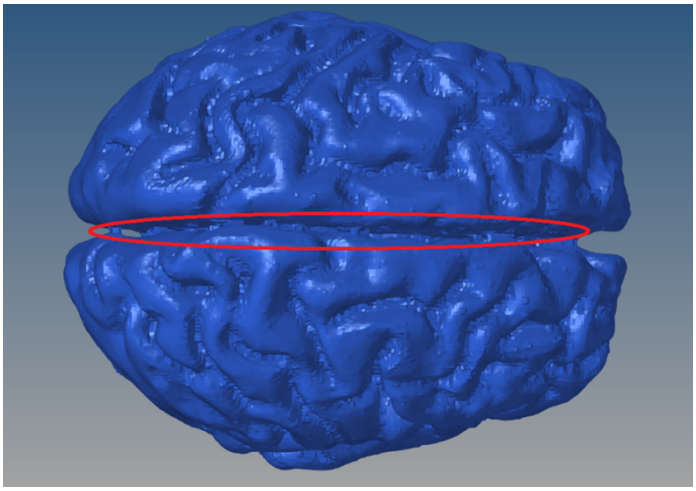

Figure 3.3: Geometry failure, the elements connected between both hemispheres.

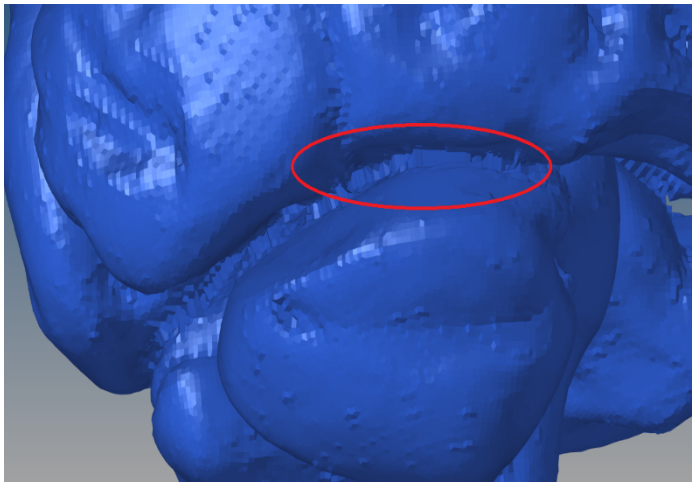

Figure 3.4: Geometry failure, the elements connected between both hemispheres and the cerebellum.

In order to solve these geometry failures, the best solution found was to separate both hemispheres and the cerebellum into three different components before running the 'Shrink Wrap Mesh' algorithm. This separation caused irregularities in the geometry, so a manual reconstruction was necessary for the areas where the three components were to be connected later. This reconstruction was carried out in such a way as to facilitate future connections. Figures 3.5-3.7 shows these 3 different components before running the algorithm.

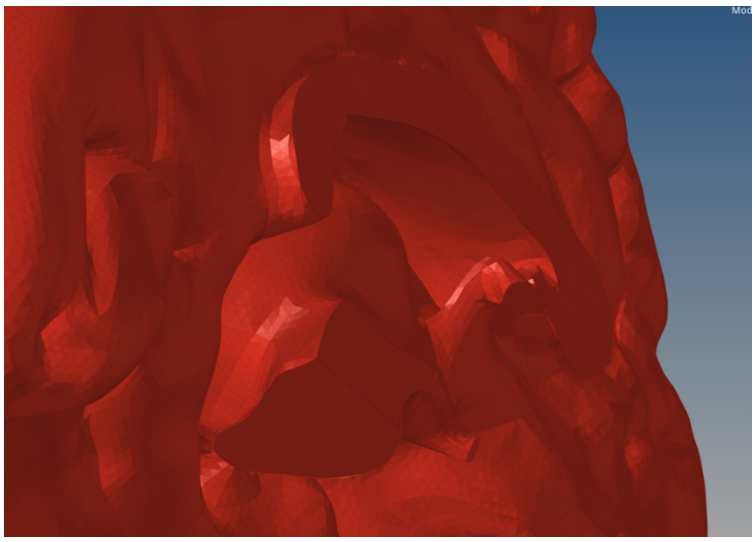

Figure 3.5: The right hemisphere before running the 'Shrink Wrap Mesh' algorithm, with flattened surfaces in Corpus Callosum and Cerebellum.

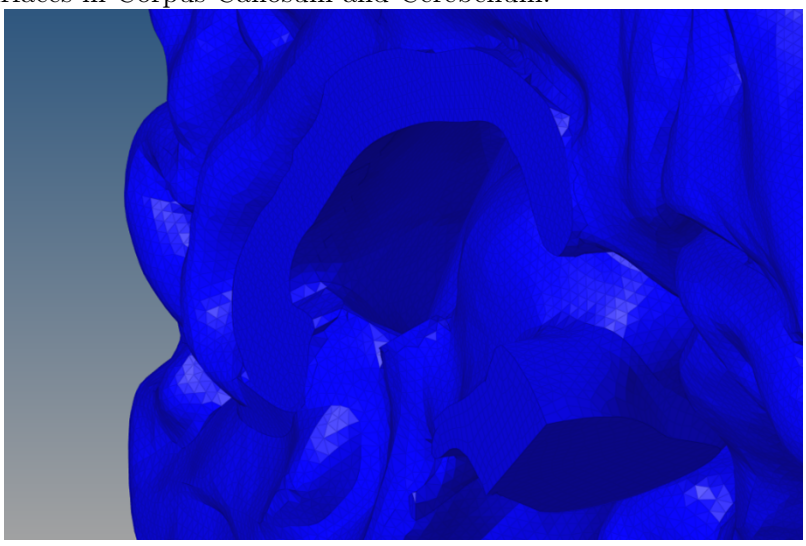

Figure 3.6: The left hemisphere before running the 'Shrink Wrap Mesh' algorithm, with flattened surfaces in Corpus Callosum and Cerebellum.

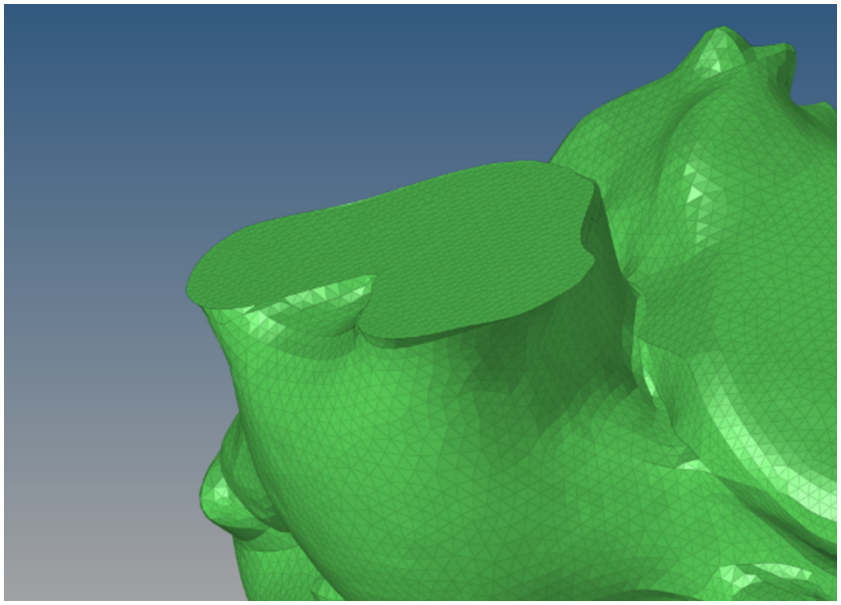

Figure 3.7: The Cerebellum before running the 'Shrink Wrap Mesh' algorithm, with flattened surface one the place where it will be connected to both hemispheres.

Having run the algorithm on all components, a manual connection was then made between them, thus obtaining the total brain in the hexahedral mesh as we can see in the following figure 3.8.

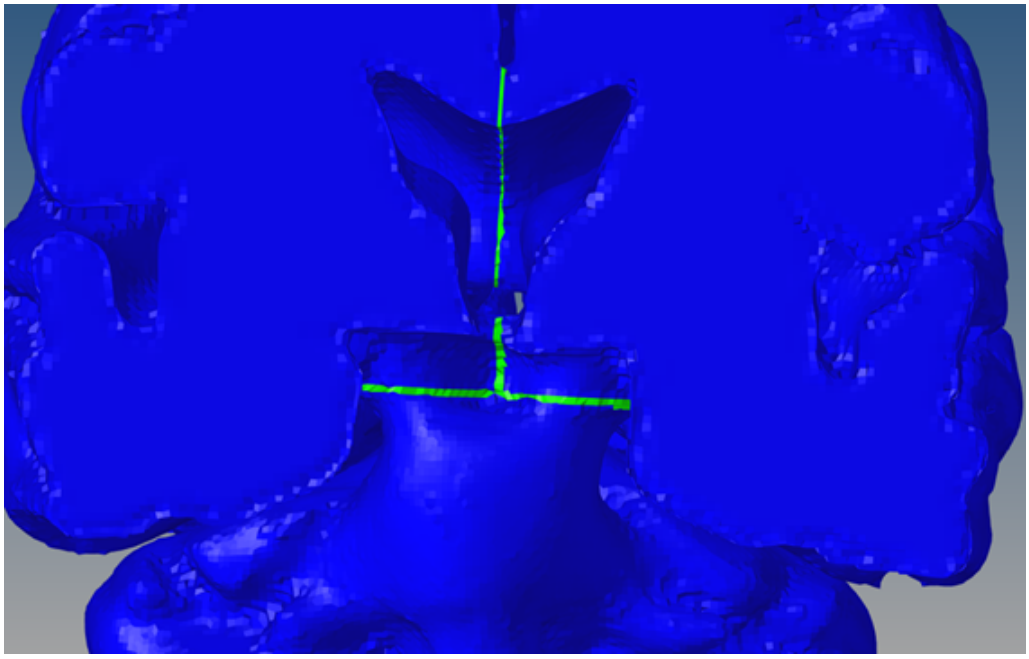

Figure 3.8: Front cut view of the brain model. All three components of the brain (blue) and the manual connections (green).

Finally, a distinction was made between white and grey matter. The thickness of the grey matter changes over a lifetime, varying between 2 and 4 mm. Winkler et all. [89] recorded an average grey matter of 2.58 mm. In this work, considering that the size imposed for each element was 1 mm, it was chosen that the three outer layers of elements of the model were designated as grey matter, since the outer layer had some flattened elements and those did have less than 1 mm of thickness, we can consider the grey matter of this model to have thickness between 2 and 3 mm as we can see in figure 3.9. For future reference, this brain model will be designated as 'Model 1'.

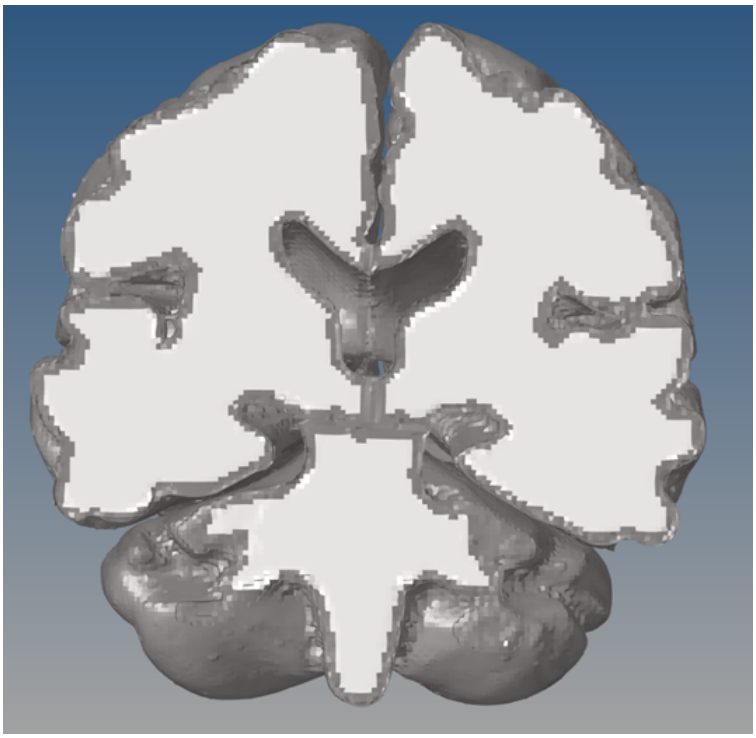

Figure 3.9: Front cut view of the brain. Grey matter (grey) and white matter (white).

3.1.2 Model 2

In addition, another hexahedral mesh brain model was created. This second model was obtained by dividing tetrahedral elements into hexahedral by a hypermesh algorithm called 'split'. In figure 3.10 the second model can be seen.

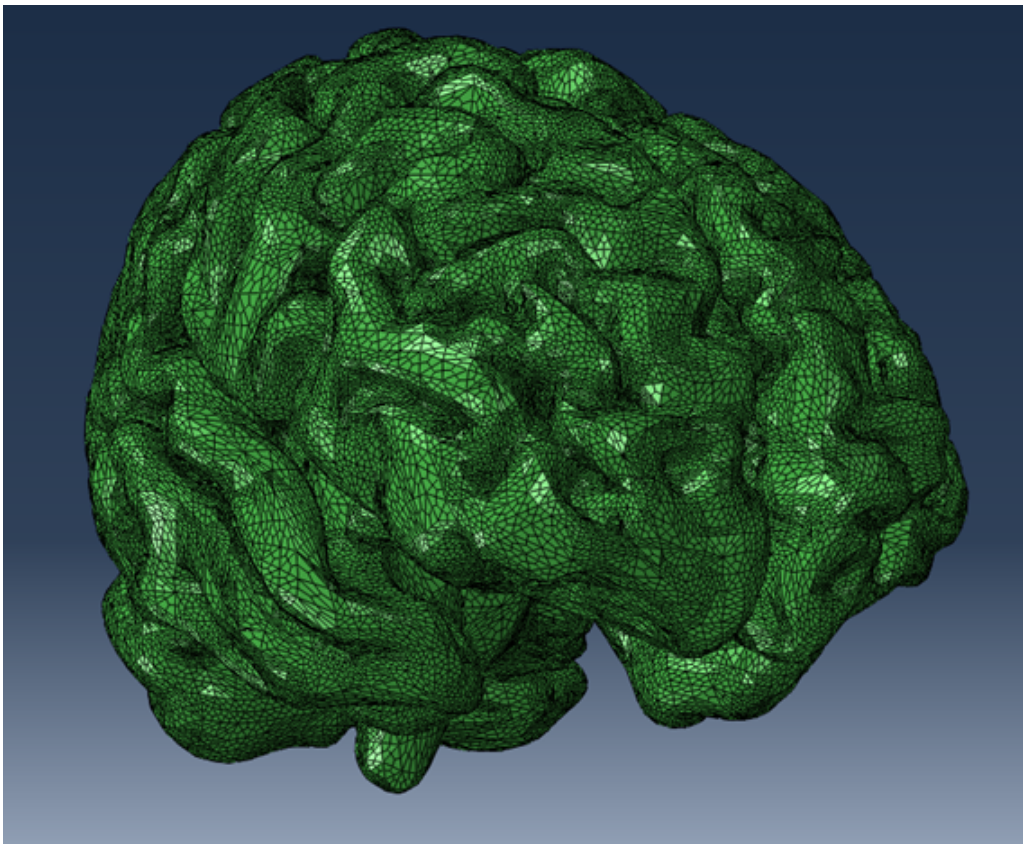

Figure 3.10: Second model with hexahedral mesh built by using the algorithm 'split'.

Although this model is easy to implement and has well-defined sulci and gyri, the average Jacobian of the elements drops considerably, and its aspect ratio goes up to double compared to the first model built with hexahedrons. In table 3.1, some characteristics regarding both models can be seen. For future reference, this brain model will be designated as 'Model 2'.

Table 3.1: Mesh properties of both models.

	N, Elements	N, Nodes	Average Jacobian	Average aspect ratio
Model 1	1367346	1462952	0.867	2.27
Model 2	720288	875358	0.22	4.32

3.2 Validation methodology

3.2.1 Hardy Experiments

The validation of both brain models will be based on Hardy et al. experiments [95]. This method of validation is commonly used to validate the motion of the brain model. These experiments consist of tracking neutral-density targets (NDTs) located on the brain's surface, using a high-speed biplanar X-ray system during different impact conditions. In Hardy experiments, a special suspension fixture was used for inverted, human cadaver head testing. This system allowed the inverted head and neck to have a rotational and translational movement as can be seen in figure 3.11.

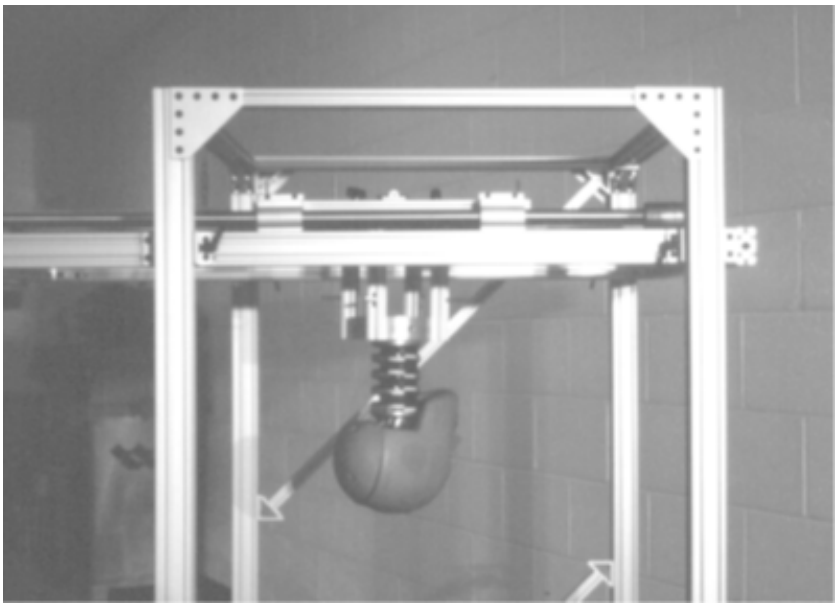

Figure 3.11: The inverted, head suspension fixture. Adapted from Hardy et al. [95].

The NDTs were implanted in two vertical columns as shown in figure 3.12. Both columns containing five or six NDTs located in the occipito-parietal and temporo-parietal regions. The columns were spaced between 7 to 12 cm.

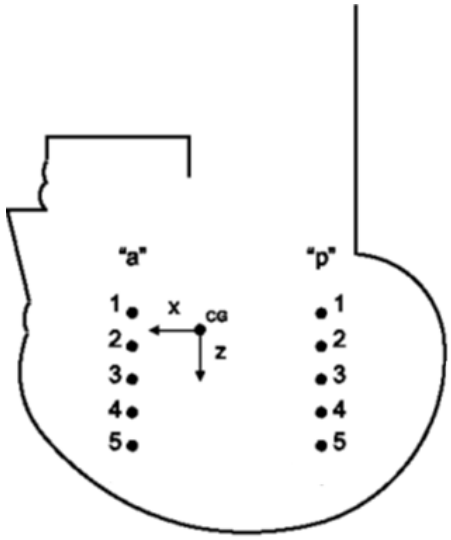

Figure 3.12: NDTs columns location used in Hardy experiments [95].

The experience chosen to validate the new brain was the C755-T2, an occipital impact with a velocity of 2 m/s. Figures 3.13 and 3.14 shows the displacement time history in X and Z directions for NDTs at both temporo-parietal and occipito-parietal regions in C755-T2 experience.

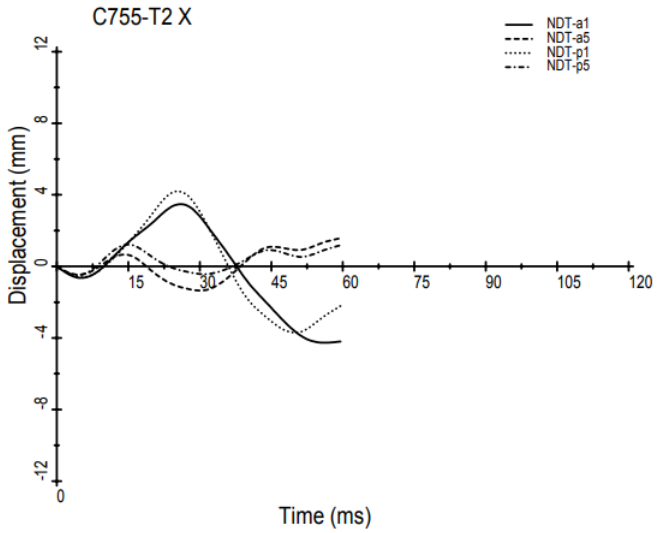

Figure 3.13: Displacement time histories for NDTs locations in the X direction for test C755-T2 [95].

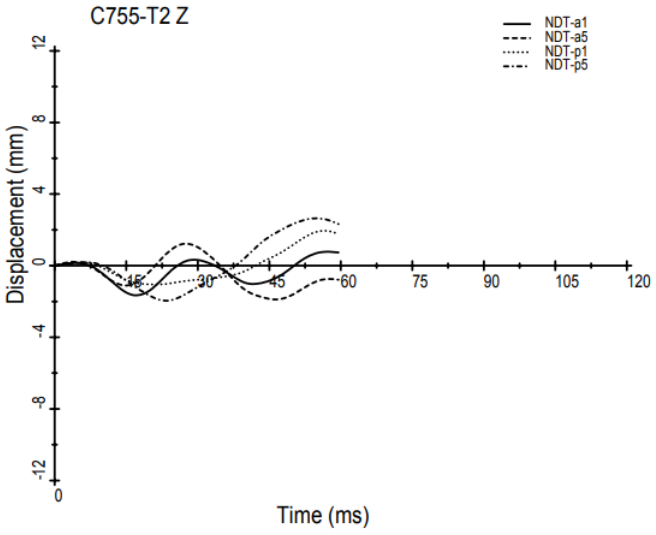

Figure 3.14: Displacement time histories for NDTs locations in the Z-direction for test C755-T2 [95].

Abaqus setup for Hardy Experiments

In order to replicate the same head motion, the exactly same kinematics measured by Hardy et al. [95] during the C755-T2 experiment, were utilized in the local coordinate system attached to the model's centre of gravity, which is the origin and a reference point of the skull. The skull was modelled as rigid for the validation and the local coordinate system moves with it. Modelling the skull as a rigid part is a plausible simplification due to the absence of skull fractures and considerable deformations. A direct impact was not simulated. Instead, the rotational and translational accelerations measured by Hardy et al. [95], were used as input for the simulation of C755-T2 experiment. The accelerations curves used to drive the model are shown in figures 3.15 and 3.16.

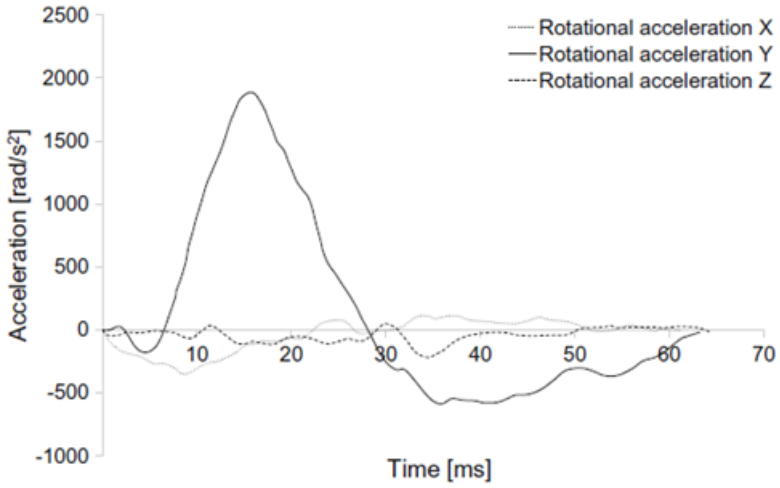

Figure 3.15: Rotational acceleration from C755-T2 experiment [95].

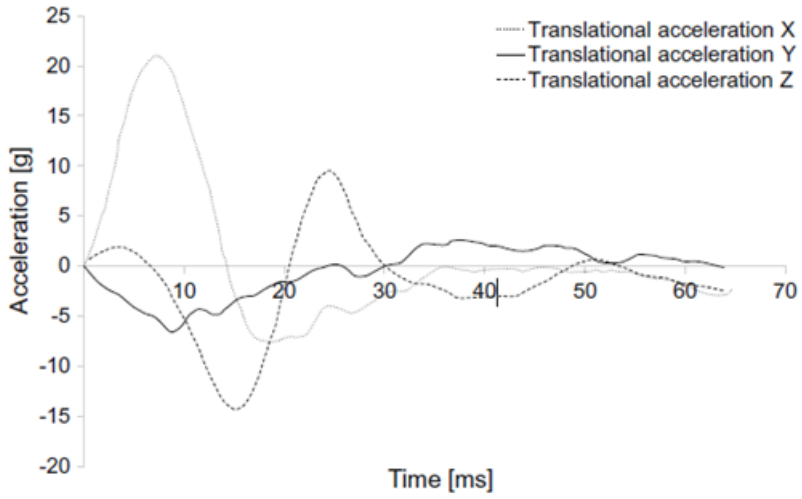

Figure 3.16: Translational acceleration from C755-T2 experiment [95].

3.2.2 Nahum Experiments

In addition, both models will also be validated based on Nahum experiments [71]. The experiment selected for this new model was the same one used to validate previously YEAHM models, Experiment 37. In the Nahum experiments, the human head suffers a blunt impact to the frontal bone in the mid-sagittal plane, the head was rotated 45° forward from the Frankfort anatomical plane. In experiment 37, a cylindrical mass of 5.59 kg hit the model at 9.94 m/s. The impactor was defined as rigid, and the padding material in its front end was modelled as a linear elastic material with a Poisson's ratio of 0.16 and Young's modulus of 6 MPa. The head model was not restrained, being able to move freely and the skull modelled as deformable. Figure 3.17 illustrates the experiment.

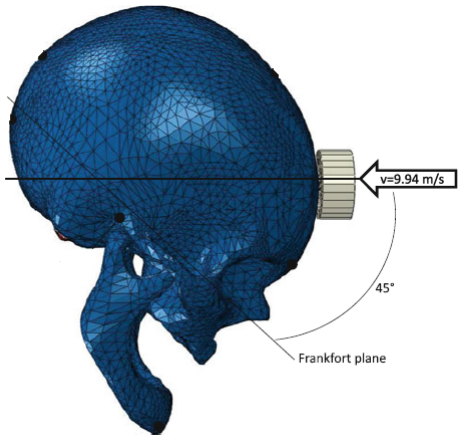

Figure 3.17: Configuration of Nahum experiment for model validation - adapted from Fernandes [3].

In these experiments, the input force and the intracranial pressure-time histories were recorded. Transducers were placed in the frontal bone, parietal bone, and in the occipital bone at the posterior fossa. The pressure in five different positions stated by Nanhum et al. [71] were used to validate this model. Nahum pressure values retrieved from Experiment 37 can be seen in figure 3.18.

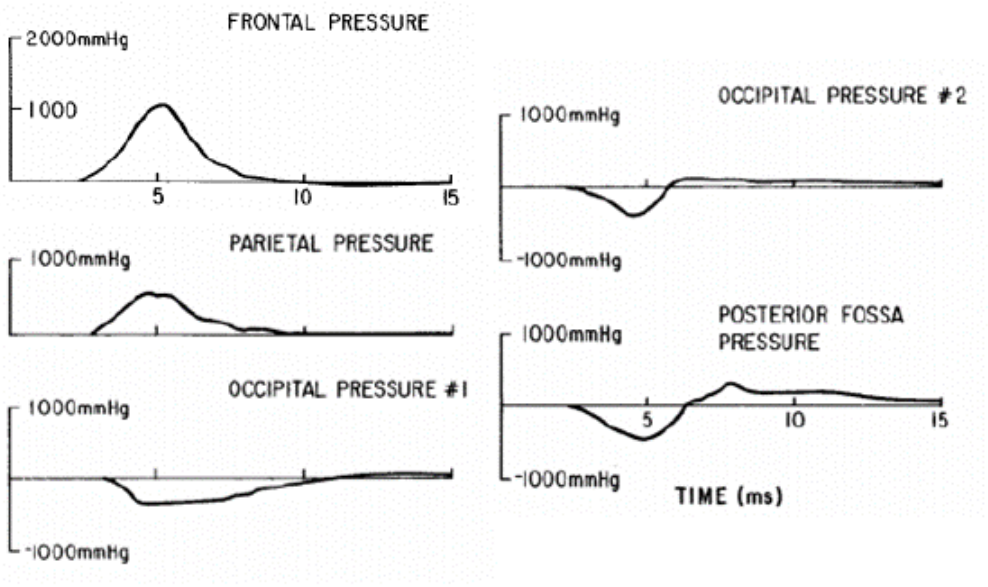

Figure 3.18: Pressure values from Experiment 37 – Retrieved from [71].

3.3 YEAHM assembly + Model 1/Model 2

After the development of the two brain models, Model 1 and Model 2, both of them were assigned the same material properties as the brain modelled by Fernandes [3]. Two assemblies were made with the remaining components of YEAHM, namely CSF and the skull developed by Fernandes [3]. Even though the last YEAHM contains the new skull model developed by Barbosa [87], the skull developed by Fernandes [3] with tetrahedral elements was used. Since the goal was to validate the brain, it was decided to reduce the complexity of the assembly in exchange for a lower computational cost, without compromising the results. Although the CSF was built on the space between the skull and the brain modelled by Fernandes [3], there were no conflicts or intersections when each brain Model was introduced in their respective assembly. The final assemblies were then constituted by the skull, CSF, and a brain model, containing a total of 1484946 elements and 1098532 elements, respectively for the assembly with Model 1 and Model 2. The assembly with Model 1 can be seen in figure 3.19.

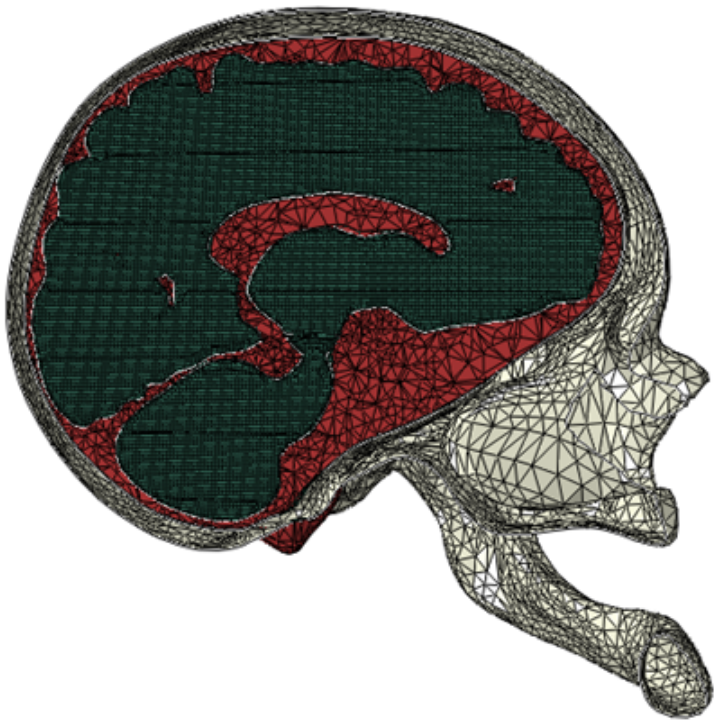

Figure 3.19: Side cut-view of the final assembly containing the skull (grey), CSF (red) and Model 1 (green).

Chapter 4

Simulation and results

All the simulations were carried out using dynamic explicit analysis performed in Abaqus software. This type of analysis is a computationally efficient method to deal with large models with a short dynamic response time [96]. During the development of this experiment, the impact of time increment size was considered, since it influences the computational cost. The largest time increment that can be used is calculated by Abaqus and it is referred to as the stable time increment. The element with the smallest stable time increment determines the time increment for the entire analysis, a review was made to check for the most critical elements and removed them. This had the effect of reducing the overall time of the simulations.

Simulations were done on a computer with an AMD Ryzen 7 5800X processor using 14 cores. The interaction between the parts was considered as a general contact with a penalty contact type with a friction coefficient of 0.2. To compare the various results from the simulations with the experiments, the acquisition of the experimental data in form of curves was carried out with a graphreader application [97].

4.1 Validation

4.1.1 Nahum's experiment - Intracranial Pressure simulation results

As stated earlier, Model 1 and Model 2 will be compared by Nahum experiments. Model 1 was tested with two types of elements, linear hexahedral with and without reduced integration, C3D8R and C3D8 respectively, while Model 2 was tested with C3D8R. All simulations were then compared with the experimental values of Nahum and with the results obtained by Fernandes [3], who used quadratic tetrahedral elements (C3D10M). Graphs with the general values obtained are shown in figures 4.1-4.5.

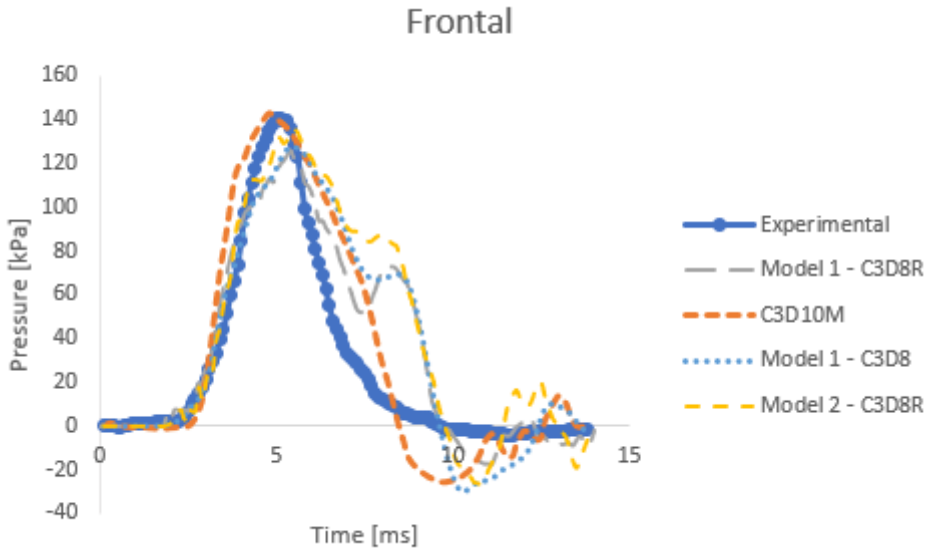

Figure 4.1: Comparison of frontal pressure between experimental and numerical results.

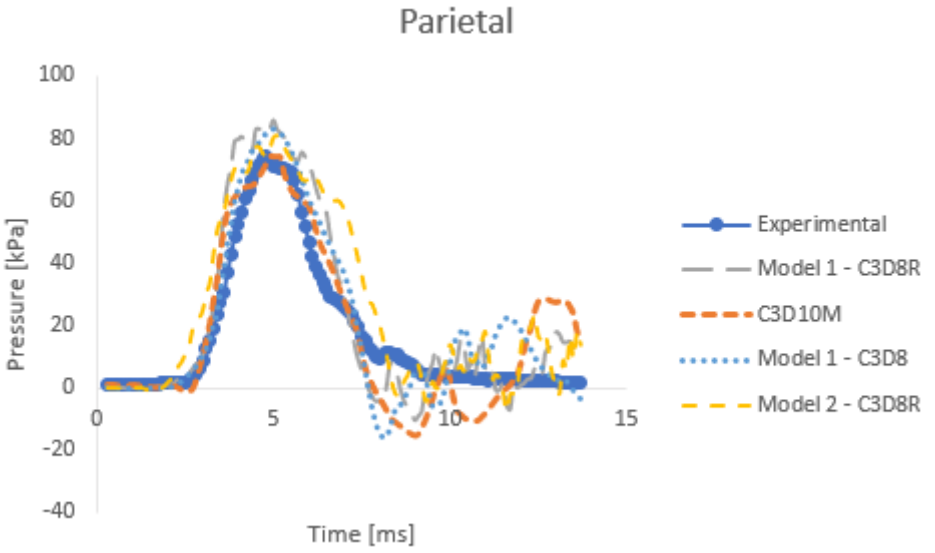

Figure 4.2: Comparison of parietal pressure between experimental and numerical results.

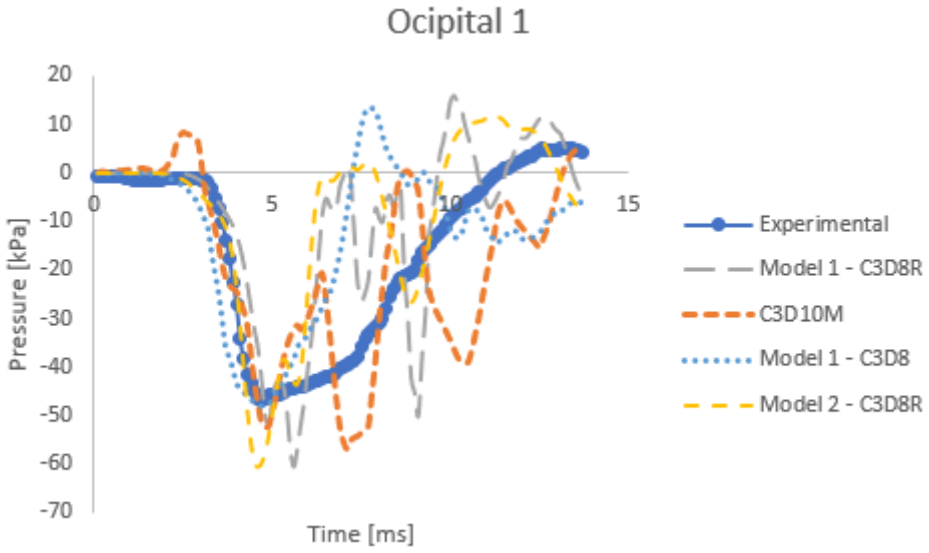

Figure 4.3: Comparison of ocipital pressure between experimental and numerical results.

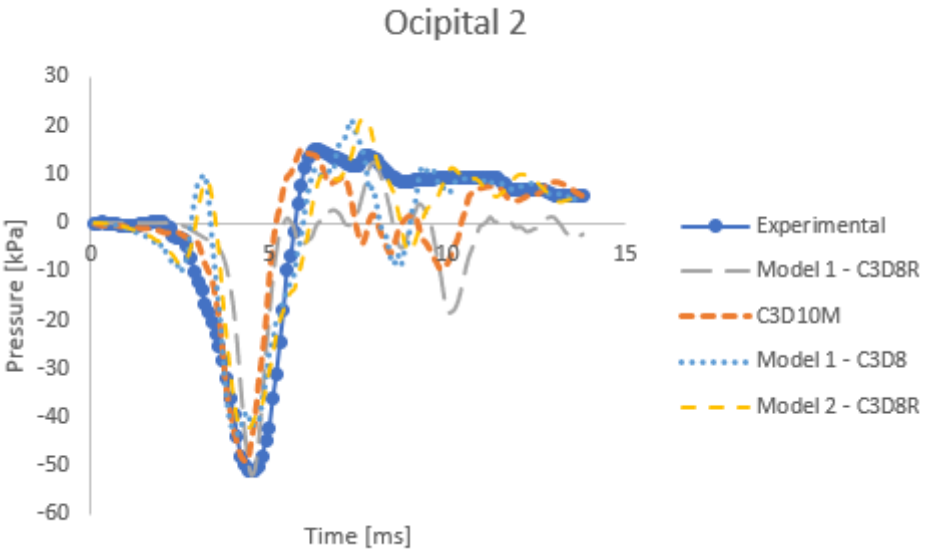

Figure 4.4: Comparison of ocipital pressure between experimental and numerical results.

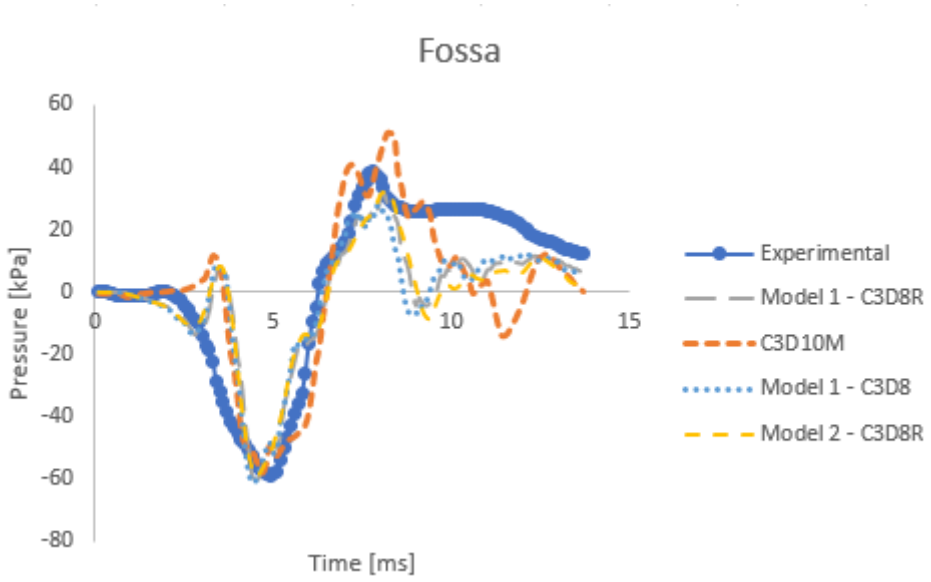

Figure 4.5: Comparison of fossa pressure between experimental and numerical results.

As can be seen, there was no great difference in the results between tetrahedral and hexahedral elements. This can be explained by the fact that the pressure in Nahum experiments is measured on the CSF elements and not directly on the brain surface. Regarding the results obtained between C3D8R and C3D8 by Model 1, the only significant difference was the operating time, as can be seen in table 4.1. The simulation with C3D8 took almost twice as long compared to the simulation with C3D8R. On the other hand, the simulation with Model 2 was the fastest, taking almost one-third of the time compared to the simulation with Model 1 using the same element(C3D8R). It also took less than half of the time compared to the simulation with C3D10M, with almost the same number of nodes. This difference in CPU time, clearly shows that the simulations with hexahedral elements are less computationally expensive than the simulations with tetrahedral elements.

Table 4.1: Comparison between different models and element types for Nahum simulations.

Model (Element Type)	N, Elements	N, Nodes	CPU Time (s)
Fernandes [3] (C3D10M)	836328	1175577	41720
Model 1 (C3D8R)	1367346	1462952	49479
Model 2 (C3D8R)	720288	875358	18608
Model 1 (C3D8)	1367346	1462952	89066

It should be noted that the results by Model 1 measured in the fossa zone, shown in figure 4.5, were virtually identical because the same element was selected from the CSF in both simulations. Thus, it is clear that the use of C3D8 or C3D8R elements did not affect the final results.

As stated previously, values were taken from the CSF and not from the brain surface, leading to the values measured for the three models (Model 1, Model 2, Fernandes [3]) producing a slight difference between them. So, the pressure values exerted on the brain were analyzed during the simulation. The three images shown in figure 4.6 were taken at the same step time, soon after the impactor hit the skull, with the same pressure limits imposed. It is clear that the pressure values obtained with hexahedral models were more homogeneous and its propagation was smoother than the C3D10M model. It also shows the difficulty in creating a hexahedral mesh in such a complex geometry, as can be seen in the lacking of an accurate representation of the sulci in Model 1 compared to Model 2, which was derived from a tetrahedral mesh. The lack of well-defined sulci, lead to some inaccurate results in the sulci regions in contrast with the rest of the brain.

In terms of brain pressure gradient, the obtained results were also similar to those obtained by Fernandes [3], who used quadratic tetrahedral elements (C3D10M). Figures 4.7 and 4.8 show pressure gradients across the brain, showing coup and contrecoup phenomenons during the simulation of Nahum's experiment with Model 1 using C3D8R.

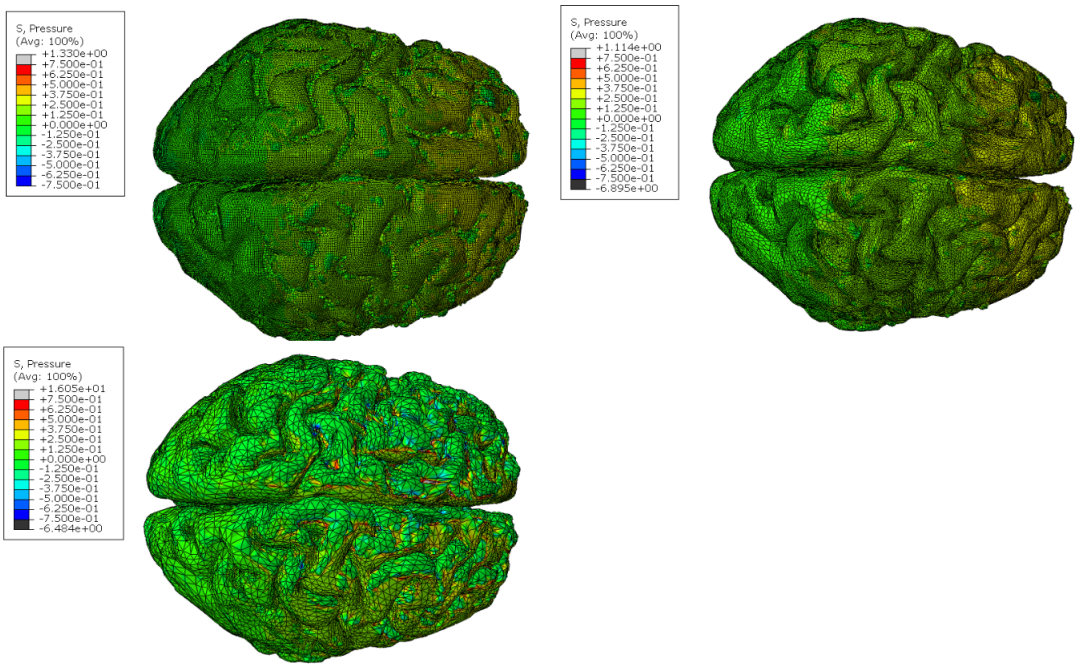

Figure 4.6: Pressure values obtained in the brain surface at 4ms for Model 1 (Top-left), Model 2 (Top-right) and Model with C3D10M (Bottom-left) (hydrostatic pressure [MPa]).

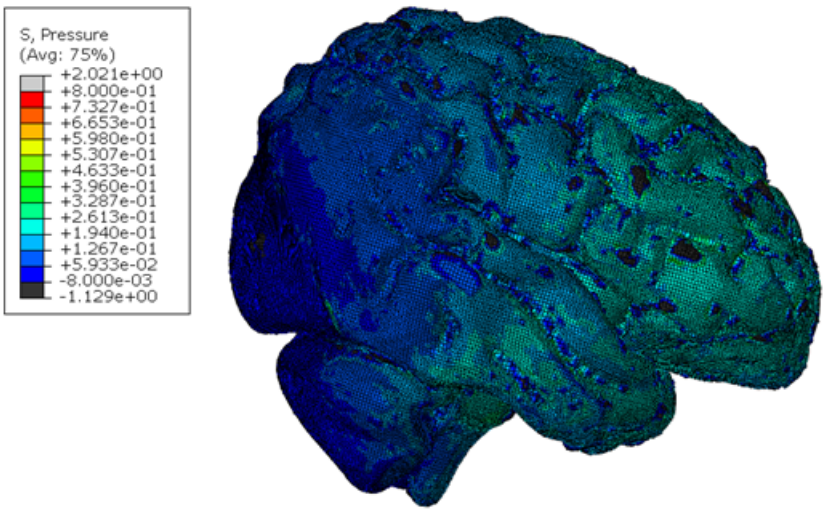

Figure 4.7: Representation of Coup phenomenon obtained by Model 1 with C3D8R (hydrostatic pressure [MPa]).

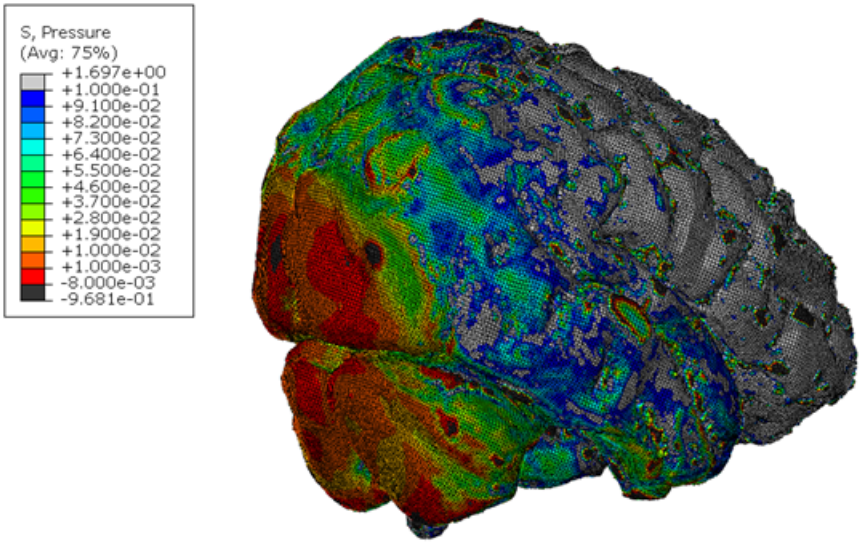

Figure 4.8: Representation of Countreoup phenomenon obtained by Model 1 with C3D8R (hydrostatic pressure [MPa]).

4.1.2 Hardy's Experiment - Brain Motion simulation results

The Hardy experiment is commonly used to validate the motion in brain models. The simulation for experiment C755-T2 was conducted for both models, Model 1 and Model 2, and the brain motion data of the selected nodes were compared with the experimental NDTs displacement. To obtain the results of displacements according to hardy's experiences, it was necessary to create a new coordinate system. This system is positioned in the skull's COG and would follow the model's movement during the simulation. This new axis system can be seen in figure 4.9.

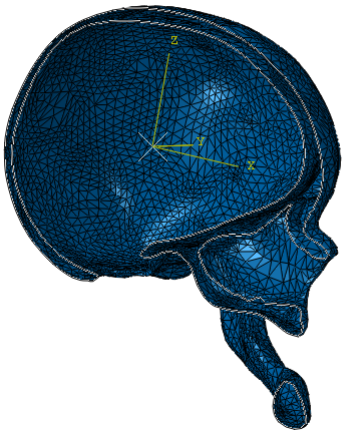

Figure 4.9: Side cut-view of the skull, showing the new coordinate system.

With this new axis system, it was possible to obtain the results of the displacements in the X and Z axes and compare them with the experimental values obtained by Hardy and with those obtained by Fernandes [3], who used quadratic linear elements (C3D10M). Model 1 was tested with two types of elements, C3D8R and C3D8. Model 2, on the other hand, was tested only with C3D8R elements. The brain model nearest nodes to the position of NDTs in the brain surface were chosen to analyse the brain displacement during the simulation. Simulation results for the relative displacement of five NDT positions in the X and Z directions for the C755-T2 test are shown in figures 4.10-4.29.

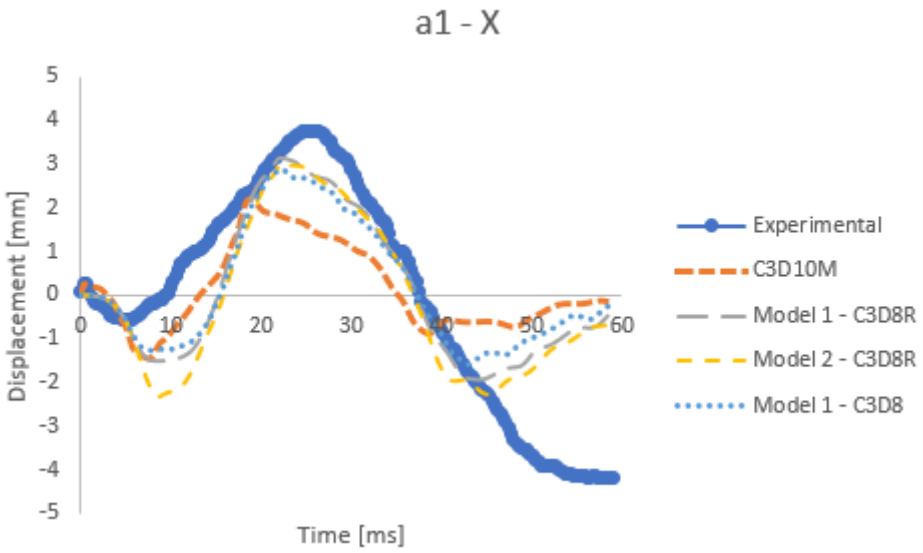

Figure 4.10: Comparison of displacement-time histories, measured at a1 in the X-direction, between experimental and numerical results.

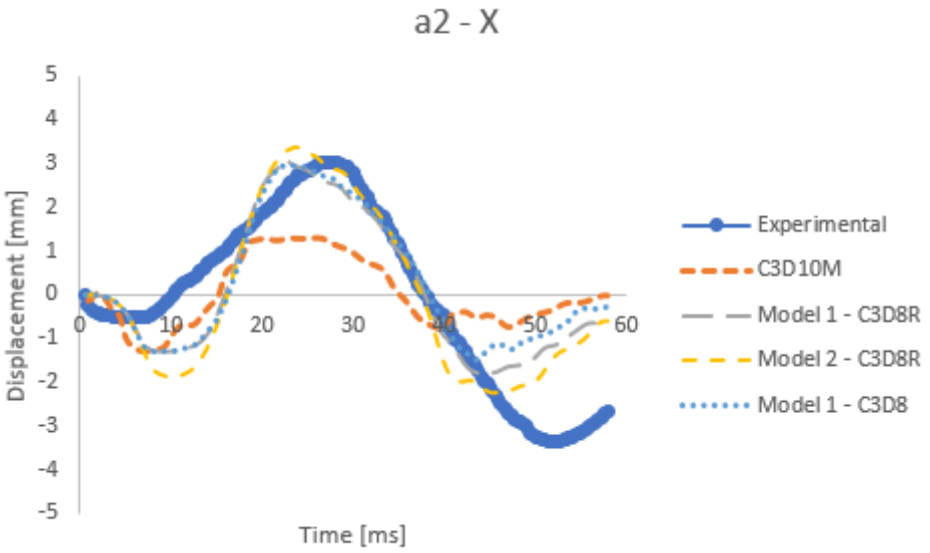

Figure 4.11: Comparison of displacement-time histories, measured at a2 in the X-direction, between experimental and numerical results.

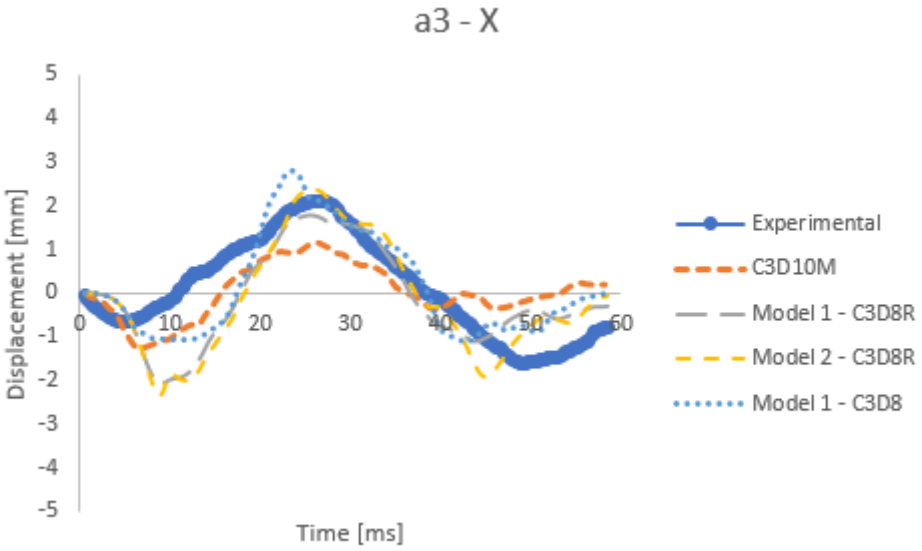

Figure 4.12: Comparison of displacement-time histories, measured at a3 in the X-direction, between experimental and numerical results.

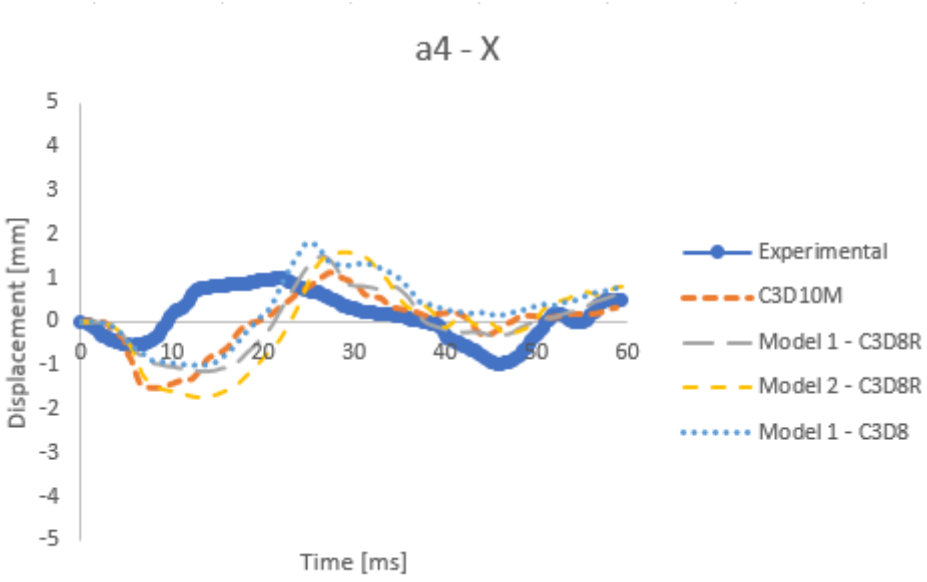

Figure 4.13: Comparison of displacement-time histories, measured at a4 in the X-direction, between experimental and numerical results.

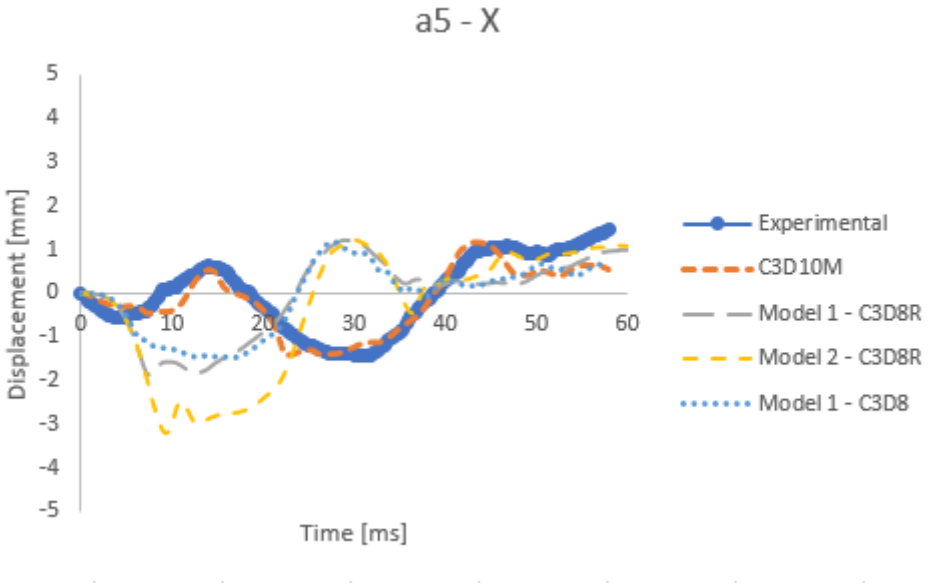

Figure 4.14: Comparison of displacement-time histories, measured at a5 in the X-direction, between experimental and numerical results.

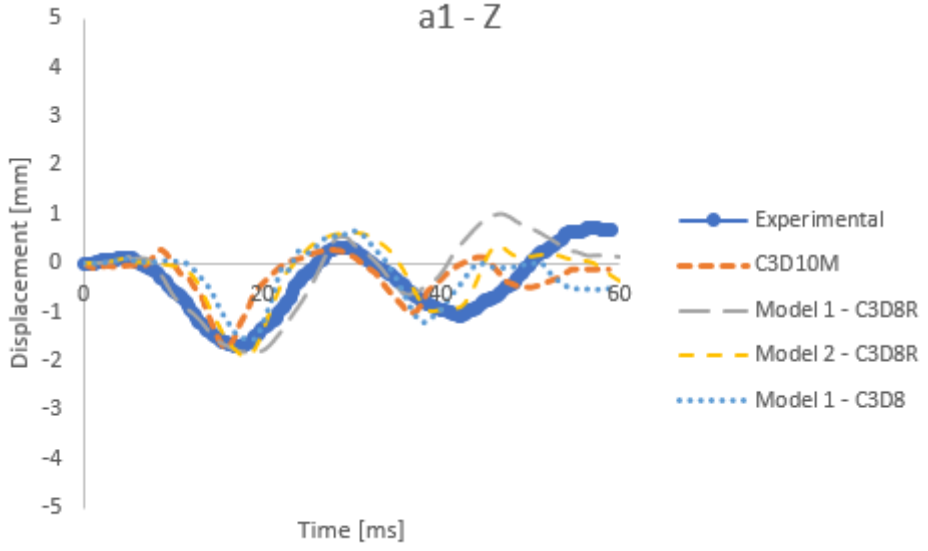

Figure 4.15: Comparison of displacement-time histories, measured at a1 in the Z-direction, between experimental and numerical results.

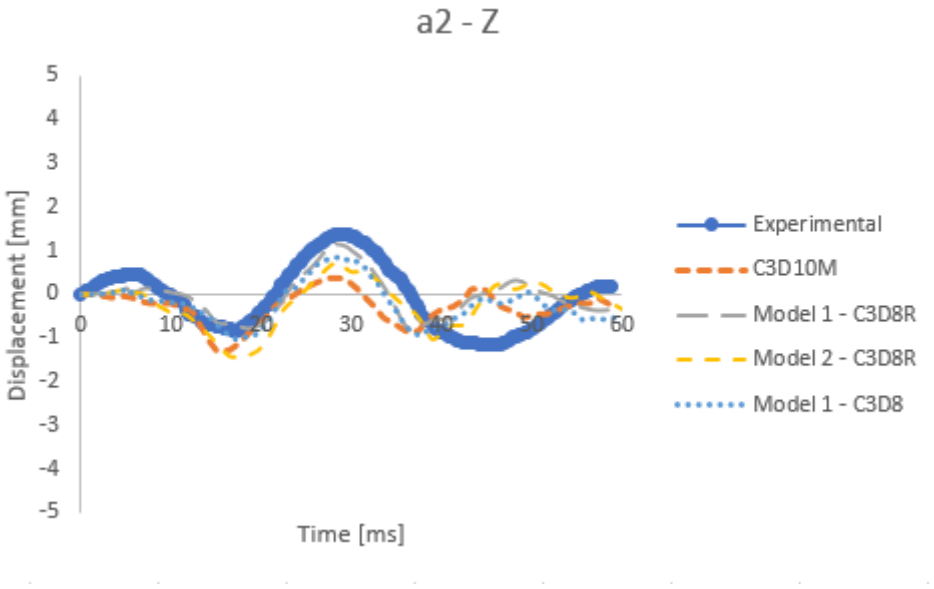

Figure 4.16: Comparison of displacement-time histories, measured at a2 in the Z-direction, between experimental and numerical results.

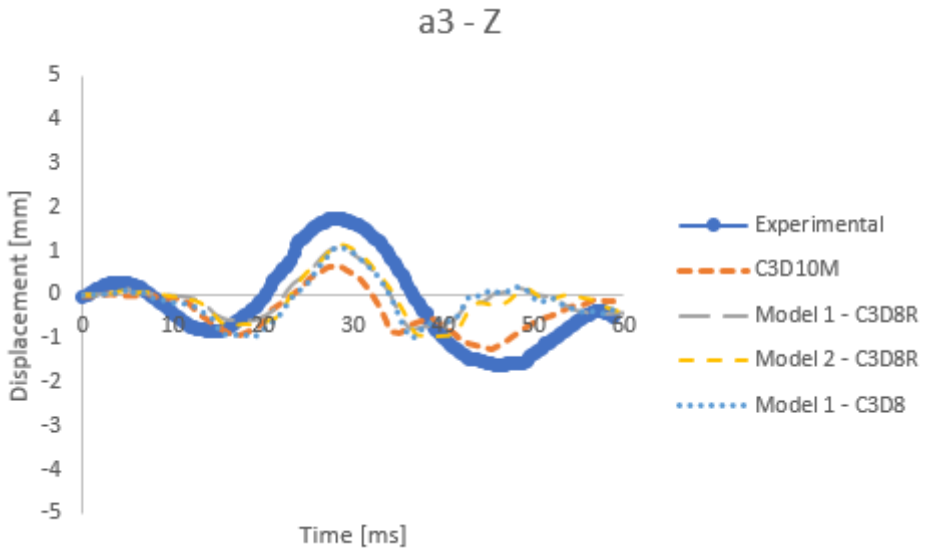

Figure 4.17: Comparison of displacement-time histories, measured at a3 in the Z-direction, between experimental and numerical results.

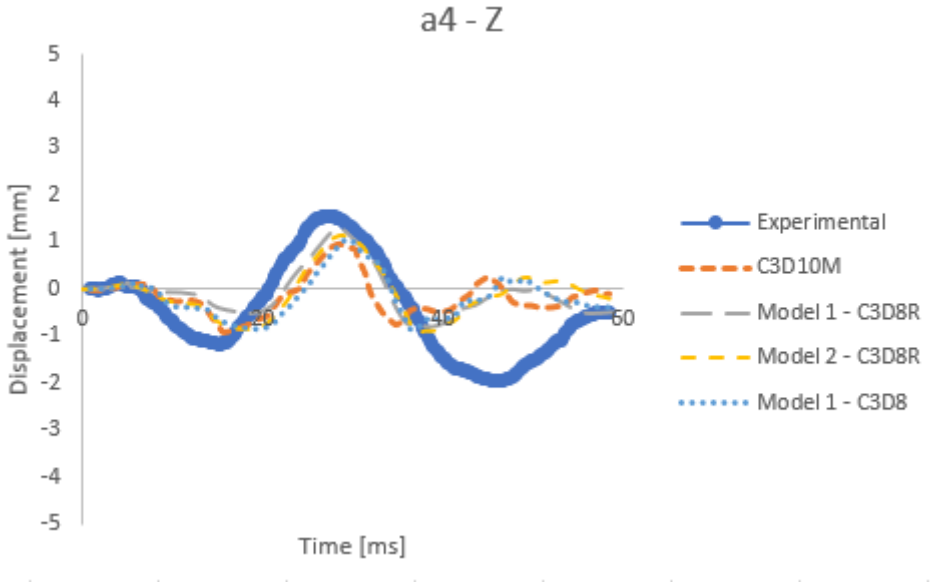

Figure 4.18: Comparison of displacement-time histories, measured at a4 in the Z direction, between experimental and numerical results.

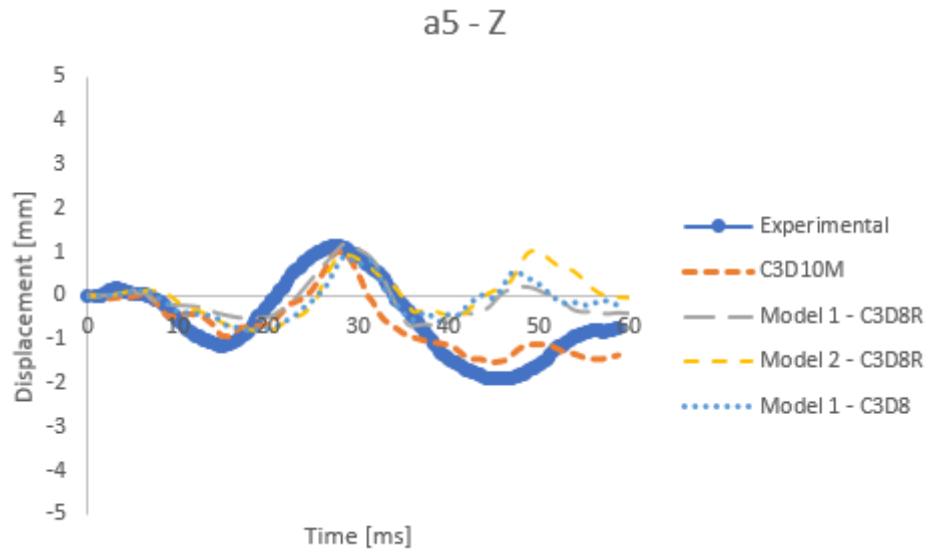

Figure 4.19: Comparison of displacement-time histories, measured at a5 in the Z-direction, between experimental and numerical results.

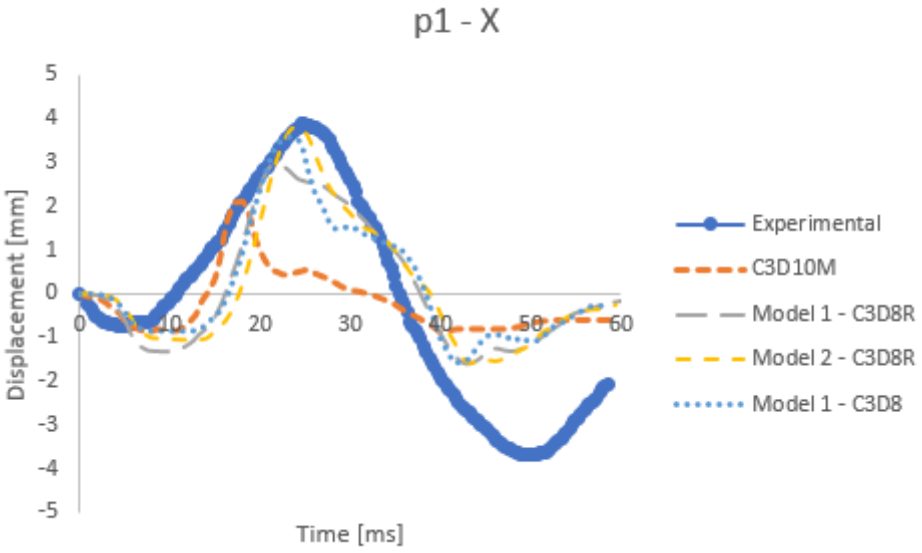

Figure 4.20: Comparison of displacement-time histories, measured at p1 in the X-direction, between experimental and numerical results.

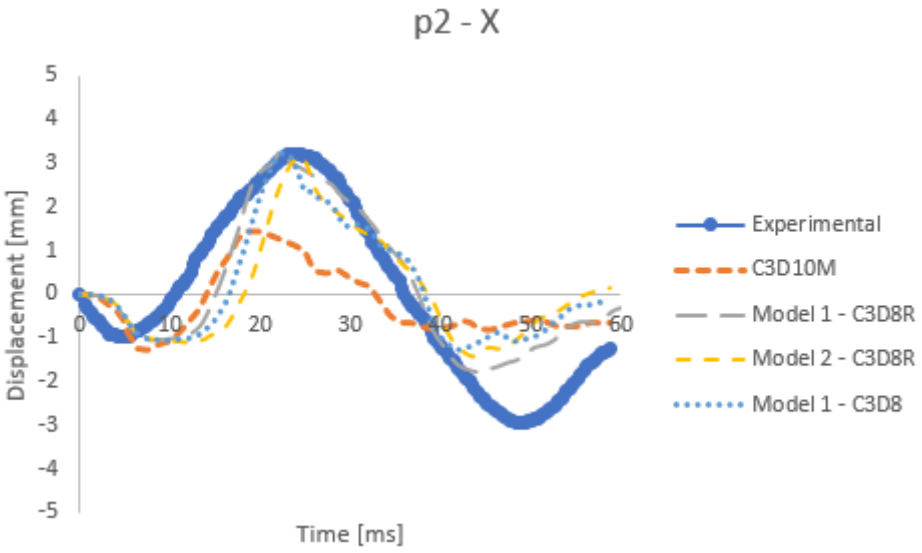

Figure 4.21: Comparison of displacement-time histories, measured at p2 in the X-direction, between experimental and numerical results.

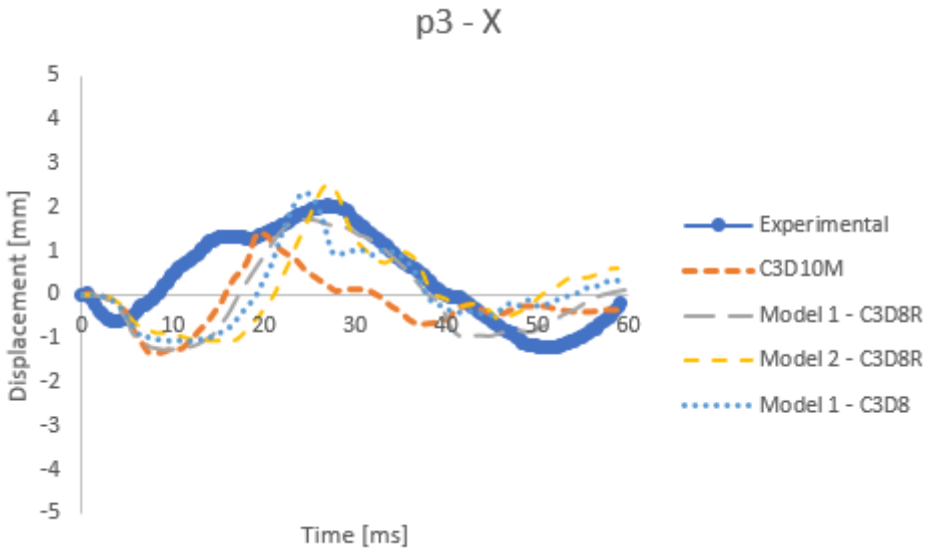

Figure 4.22: Comparison of displacement-time histories, measured at p3 in the X-direction, between experimental and numerical results.

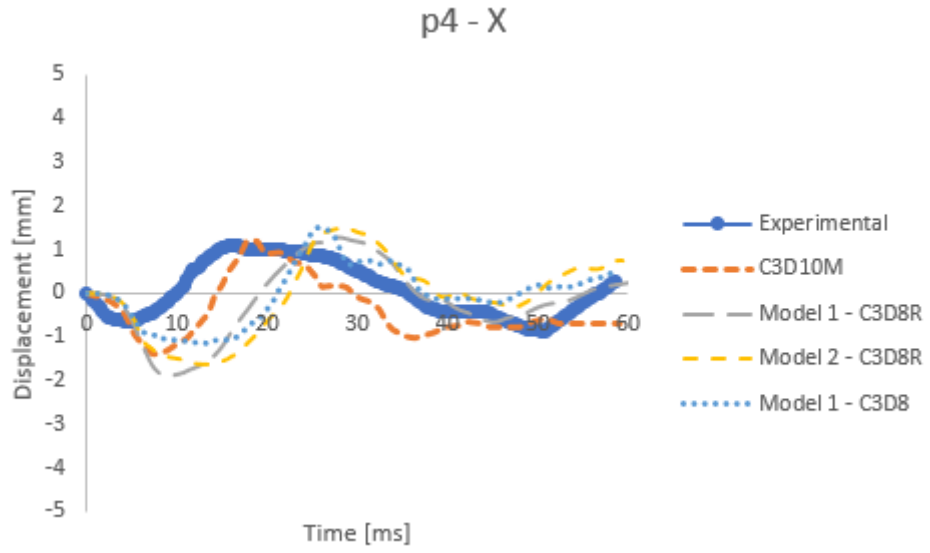

Figure 4.23: Comparison of displacement-time histories, measured at p4 in the X-direction, between experimental and numerical results.

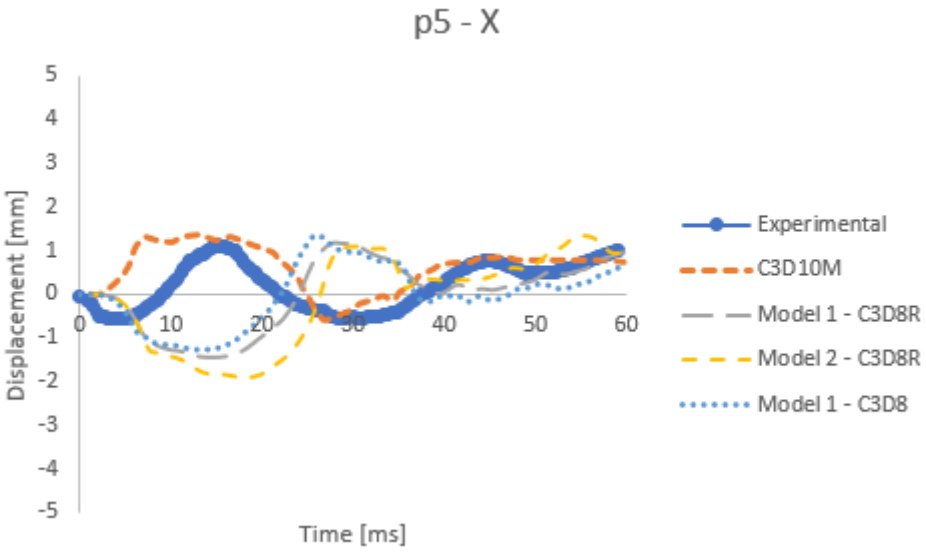

Figure 4.24: Comparison of displacement-time histories, measured at p5 in the X-direction, between experimental and numerical results.

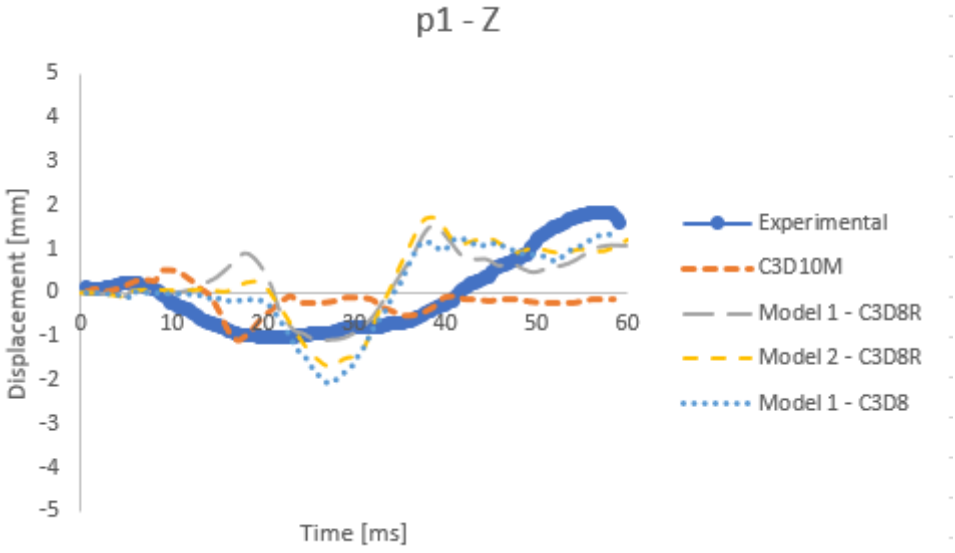

Figure 4.25: Comparison of displacement-time histories, measured at p1 in the Z-direction, between experimental and numerical results.

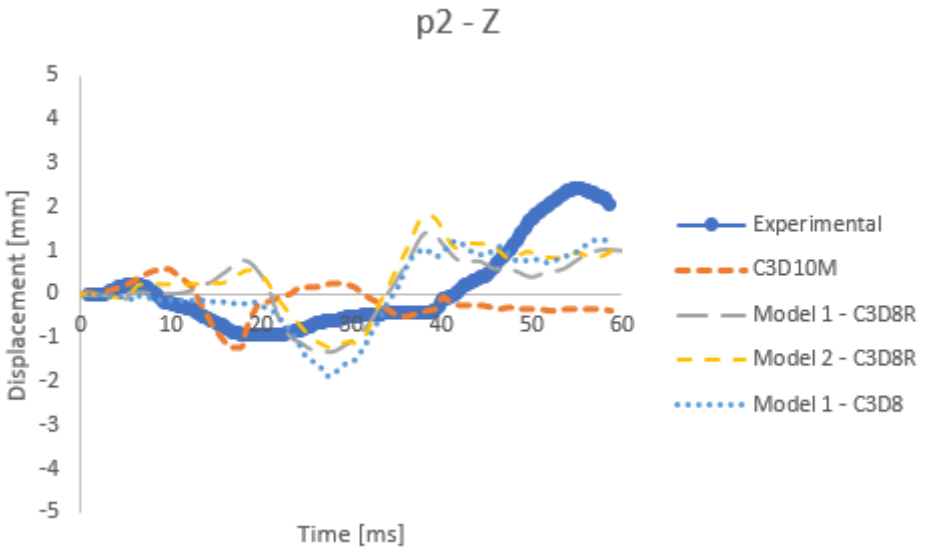

Figure 4.26: Comparison of displacement-time histories, measured at p2 in the Z-direction, between experimental and numerical results.

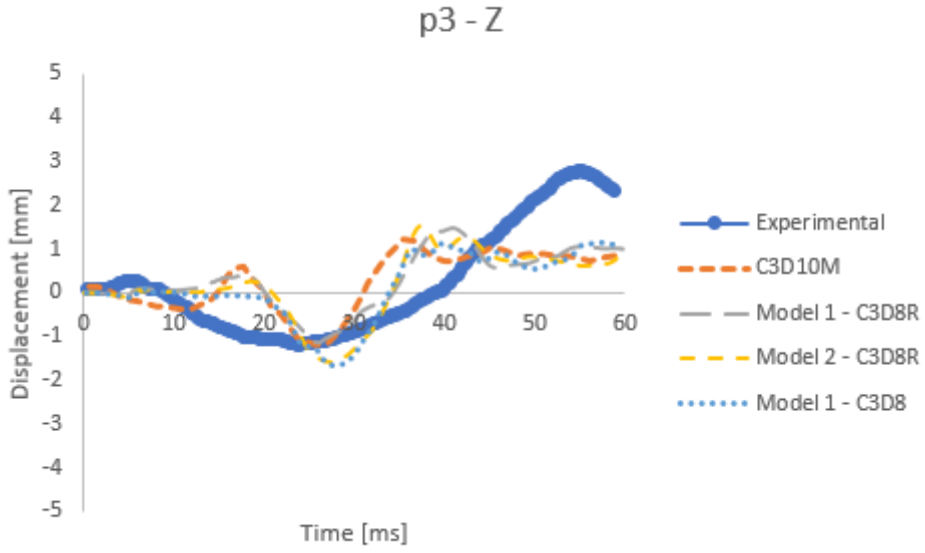

Figure 4.27: Comparison of displacement-time histories, measured at p3 in the Z-direction, between experimental and numerical results.

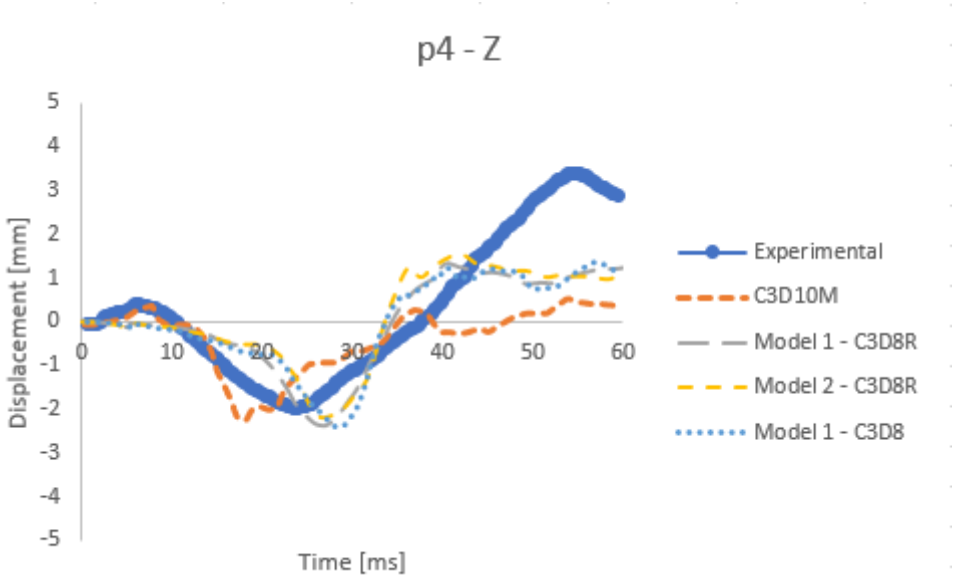

Figure 4.28: Comparison of displacement-time histories, measured at p4 in the Z-direction, between experimental and numerical results.

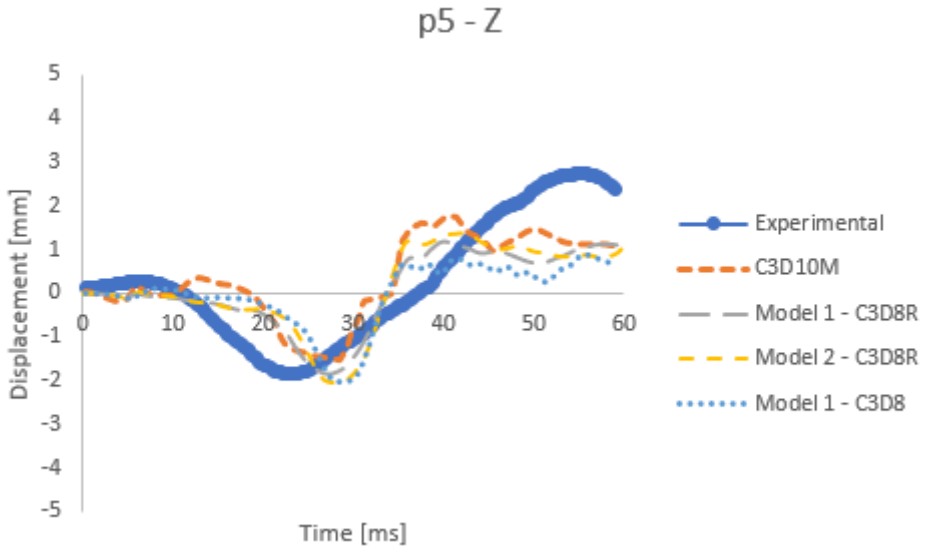

Figure 4.29: Comparison of displacement-time histories, measured at p5 in the Z-direction, between experimental and numerical results.

Overall, the simulations with hexahedral elements produced better results compared to the tetrahedral model (C3D10M). The most evident results appear at Points A1, A2, P1 and P2 in the X direction, illustrated in Figures 4.10-4.11; 4.20-4.21 respectively. The results of Model 1 with C3D8R and C3D8, as well as Model 2 with C3D8R, always manage to reach the peak displacement obtained by Hardy's experimental results. On the other hand, the results obtained with C3D10M could not reach displacement values higher than 2mm. Regarding the results obtained in the Z-direction, as shown in Figures 4.15-4.19; 4.25-4.29, they are very similar in all simulations. This shows that the use of hexahedral elements can lead to the same results as the use of tetrahedral elements in the Z-direction. Note that the results gain a certain delay in time, according to the X direction, compared to Hardy's experimental values. The delay values increase from [A1-A5] and from [P1-P5], as demonstrated in figures 4.10-4.14; 4.20-4.24, reaching significant values above 10 ms at the highest points (A4, A5, P4, P5). According to the presented results, the simulation with Model 2 using C3D8R elements had the highest delay values compared to the other simulations.

As table 4.2 shows, the simulation with C3D8 was the longest in terms of computational cost. It required almost twice as much time as the simulation with C3D8R. Since the results in both simulations are very similar, it is safe to discard the simulations with C3D8 elements in future projects. The simulation of Model 2 with C3D8R elements was the fastest. It required only about one-third the time of the simulation of Model 1 with the same element type. Although Model 2 contains the worst Jacobian elements, it is not fair to compare it to Model 1 because it contains almost half of the nodes.

Table 4.2: Comparison between different models and element types for Hardy simulations.

Model (Element Type)	N, Elements	N, Nodes	CPU Time (s)
Fernandes [3] (C3D10M)	836328	1175577	87228
Model 1 (C3D8R)	1367346	1462952	127336
Model 2 (C3D8R)	720288	875358	38561
Model 1 (C3D8)	1367346	1462952	203436

Chapter 5

Conclusion and future work

In this dissertation, two computational models of the brain of a 65-year-old man were developed and integrated into the YEAHM. Both brain models were then validated using two experiments, the cadaveric impacts performed by Nahum [90] and by Hardy [89].

To this end, the literature was reviewed to gain an understanding of the various components of the human head, the assessment of head trauma, and the history of finite element head models and their properties. The main focus of this study was the brain, a review was made from thresholds for TBI to material properties and types of finite elements used for the brain throughout the history of FEHM.

Thus, the main objective was to create a hexahedral mesh for the brain and compare it to the existing tetrahedral mesh. Different elements were simulated for both models to evaluate which one produced better results in terms of, computational cost, precision and geometry resemblance.

The simulations performed by Model 2, using hexahedral elements with reduced integration, proved to be less computationally expensive than those made with quadratic tetrahedral elements while providing better results. In both experiments, the simulations with Model 2 required less than half the time compared to those by C3D10M while having only 13% fewer nodes. Even tough it is not a linear problem, there was a significant reduction in time, compared to the small reduction of number in nodes.

Although the development of Model 1 was more complicated, the brain motion was smooth throughout the simulations, achieving great results. On the other hand, Model 2 was a much easier hexahedral mesh to build, without compromising its purpose.

5.1 Future works

Although the YEAHM model already has a high level of complexity and contains various parts such as the skull, brain, CSF, SSS, and connecting veins. It would be a great improvement to split the current CSF into all its components, namely the dura, arachnoid and pia mater to achieve a more realistic model. This division will also have a great impact on future studies because the meninges are an important part of the human head model to mitigate and transfer damage to the brain.

Also regarding the CSF component, since the goal is to make it more realistic, it is suggested to model the CSF with the coupled eulerian lagrangian method or with the smooth particle hydrodynamic method.

Considering the hexahedral brain models developed in this dissertation, one suggestion is to add them to the complete YEAHM model, which includes the skull developed by Barbosa [87], the bridging veins, and the SSS developed by Costa [86].

Lastly, since the brain model is now divided into grey and white matter, it would be advantageous to test different material properties for each component, adding one more layer of complexity to YEAHM to achieve even better results.

Bibliography

[1] K. O'Keefe, "Traumatic brain injury," *Emergency Medical Services: Clinical Practice and Systems Oversight: Second Edition*, vol. 1, pp. 237–242, 2015.

[2] K. M. Tse, S. P. Lim, V. B. C. Tan, and H. P. Lee, "A review of head injury and finite element head models," *American Journal of Engineering*, vol. 1, no. 5, pp. 28–52, 2014.

[3] F. A. Fernandes, D. Tchepel, R. J. Alves de Sousa, and M. Ptak, "Development and validation of a new finite element human head model: Yet another head model (YEAHM)," *Engineering Computations (Swansea, Wales)*, vol. 35, no. 1, pp. 477–496, 2018.

[4] W. J. Hamilton, *Anatomy for students*, vol. 4. 1969.

[5] P. A. School, ""The skull bones and features,"." `http://paletteartschool.com/tutorials/the-skull-bones-and-features/`. Accessed: 20-04-2021.

[6] Lumenlearning, "The Bones of the Skull." `https://courses.lumenlearning.com/ap1x94x1/chapter/the-bones-of-the-skull/`. Accessed: 20-04-2021.

[7] B. w. Site, ""Human Anatomy and Physiology Lab (BSB 141),"."

[8] S. Jacobson and E. M. Marcus, *Neuroanatomy for the neuroscientist*. Springer US, 2008.

[9] I. Decimo, G. Fumagalli, V. Berton, M. Krampera, and F. Bifari, "Meninges: From protective membrane to stem cell niche," *American Journal of Stem Cells*, vol. 1, no. 2, pp. 92–105, 2012.

[10] AANS, "Anatomy of the Brain." `https://www.aans.org/en/Patients/Neurosurgical-Conditions-and-Treatments/Anatomy-of-the-Brain`. Accessed: 26-04-2021.

[11] N. M. Borden, S. E. Forseen, C. Stefan, and A. J. E. Moore, *Imaging Anatomy of the Human Brain*. 2015.

[12] R. Carter, S. Aldridge, M. Page, and S. Parker, *The human brain book: An illustrated guide to its structure, function, and disorders*. 2019.

[13] S. C. Authors, N. Of, and A. At, *II. Anatomy and physiology*, vol. 19. 1934.

[14] T. H. E. Human and F. Lobes, *The Human Frontal Lobes: Functions and Disorders, 2nd ed*, vol. 65. 2008.

[15] Q. B. Institute, "Lobes of the brain." `https://qbi.uq.edu.au/brain/brain-anatomy/lobes-brain`. Accessed: 29-04-2021.

[16] R. Joseph, *The Parietal Lobes*. 1990.

[17] J. W. Bisley and M. E. Goldberg, "Attention, intention, and priority in the parietal lobe," *Annual Review of Neuroscience*, vol. 33, pp. 1–21, 2010.

[18] L. Fogassi and G. Luppino, "Motor functions of the parietal lobe," *Current Opinion in Neurobiology*, vol. 15, no. 6, pp. 626–631, 2005.

[19] S. Sveinbjornsdottir and J. S. Duncan, "Parietal and occipital lobe epilepsy: a review [published erratum appears in Epilepsia 1994 Mar-Apr;35(2):467]. [Review]," *Epilepsia*, vol. 34, no. 3, pp. 493–521, 1993.

[20] S. Budday, T. C. Ovaert, G. A. Holzapfel, P. Steinmann, and E. Kuhl, *Fifty Shades of Brain: A Review on the Mechanical Testing and Modeling of Brain Tissue*, vol. 27. Springer Netherlands, 2019.

[21] S. Budday, G. Sommer, C. Birkl, C. Langkammer, J. Haybaeck, J. Kohnert, M. Bauer, F. Paulsen, P. Steinmann, E. Kuhl, and G. A. Holzapfel, "Mechanical characterization of human brain tissue," *Acta Biomaterialia*, vol. 48, pp. 319–340, 2017.

[22] J. E. Galford and J. H. McElhaney, "A viscoelastic study of scalp, brain, and dura," *Journal of Biomechanics*, vol. 3, no. 2, pp. 211–221, 1970.

[23] S. Chatelin, A. Constantinesco, and R. Willinger, "Fifty years of brain tissue mechanical testing: From in vitro to in vivo investigations," *Biorheology*, vol. 47, no. 5-6, pp. 255–276, 2010.

[24] K. P. Whittall, A. L. MacKay, D. A. Graeb, R. A. Nugent, D. K. Li, and D. W. Paty, "In vivo measurement of T2 distributions and water contents in normal human brain," *Magnetic Resonance in Medicine*, vol. 37, no. 1, pp. 34–43, 1997.

[25] K. L. Thibault and S. S. Margulies, "Age-dependent material properties of the porcine cerebrum: Effect on pediatric inertial head injury criteria," *Journal of Biomechanics*, vol. 31, no. 12, pp. 1119–1126, 1998.

[26] G. McIlvain, H. Schwarb, N. J. Cohen, E. H. Telzer, and C. L. Johnson, "Mechanical properties of the in vivo adolescent human brain," *Developmental Cognitive Neuroscience*, vol. 34, no. June, pp. 27–33, 2018.

[27] K. Blennow, D. L. Brody, P. M. Kochanek, H. Levin, A. McKee, G. M. Ribbers, K. Yaffe, and H. Zetterberg, "Traumatic brain injuries," *Nature Reviews Disease Primers*, vol. 2, pp. 1–19, 2016.

[28] B. Chinn and D. Hynd, "Technical response to the unpublished paper: critical evaluation of the SHARP motorcycle helmet rating," *TRL Published Project Report*, 2009.

[29] D. H. Smith and D. F. Meaney, "Axonal damage in traumatic brain injury," *Neuroscientist*, vol. 6, no. 6, pp. 483–495, 2000.

[30] M. Aare, "Prevention of Head InjuriesSpecifically on Oblique Impacts," *Division of Neuronic Engineering*, vol. Ph. D., p. 35, 2003.

[31] D. I. Graham, J. H. Adams, J. A. Nicoll, W. L. Maxwell, and T. A. Gennarelli, "The Nature, Distribution and Causes of Traumatic Brain Injury," *Brain Pathology*, vol. 5, no. 4, pp. 397–406, 1995.

[32] J. G. Greenfield, *Greenfield's neuropathology*. 2008.

[33] C. W. Gadd, "Use of a weighted-impulse criterion for estimating injury hazard," in *Proceedings of 10th Stapp Car*, (New York), SAE Technical Paper, 1966.

[34] L. Zhang, K. H. Yang, and A. I. King, "A Proposed Injury Threshold for Mild Traumatic Brain Injury," *Journal of Biomechanical Engineering*, vol. 126, no. 2, pp. 226–236, 2004.

[35] J. Versac, "A review of severity of index," in *Proceedings of 15th Stapp Car Crash Conference*, (Warrendale), 1971.

[36] W. Goldsmith, "Current controversies in the stipulation," *Journal of Biomechanics*, vol. 14, pp. 883–884, 1981.

[37] C. S. Wood and D., "Injury mechanisms and injury criteria," in *Pedestrian and Cyclist Impact Mechanics*, (Netherlands), pp. 75–97, 2009.

[38] J. A. Newman, "A generalized acceleration model for brain injury threshold (GAMBIT)," in *Proceedings of International IRCOBI Conference on the Biomechanics of Impacts*, (Zurich), pp. 121–131, 1986.

[39] J. A. Newman, N. Shewchenko, and E. Welbourne, "A Proposed New Biomechanical Head Injury Assessment Function -The Maximum Power Index All SAE papers, standards, and selected books are abstracted and indexed in the Global Mobility Database A Proposed New Biomechanical Head Injury Assessment Function -Th," *Reprinted From: Stapp Car Crash Journal*, vol. 44, no. 724, pp. 1–35, 2000.

[40] A. M. Ward, C. C., Chan, M. and Nahum, "Intracranial pressure-a brain injury criterion.," in *Proceedings of 24th Stapp Car Crash Conference*, 1980.

[41] B. Kang, H. S., Willinger, R., Diaw, B. and Chinn, "Validation of a 3D anatomic human head model and replication of head impact in motorcycle accident by finite element modeling.," in *Proceedings of 41st Stapp Car Crash Conference*, 1997.

[42] G. Anderson, R. W. G., Brown, C. J., Blumbergs, P. C., Scott and A. J. Finney, J. W., Jones, N. R. and McLean, "Mechanisms of axonal injury: an experimental and numerical study of a sheep model of head impact.," in *Proceedings of International IRCOBI Conference on the Biomechanics of Impacts,*, 1999.

[43] L. Zhou, C., Kahlil, T. and Dragovic, "Head injury assessment of a real world crash by finite element modeling. In," in *Proceedings of Advisory Group for Aerospace Research and Development (AGARD)*, 1996.

[44] C. Miller, R. T., Margulies, S. S., Leoni, M., Nonaka, M. and D. F. X., Smith, D. H. and Meaney, "Finite element modeling approaches for predicting injury in an experimental model of severe diffuse axonal injury.," in *Proceedings of 42nd Stapp Car Crash Conference*, 1998.

[45] R. W. G. Anderson, *A study of the biomechanics of axonal injury.* PhD thesis, University of Adelaide, 2000.

[46] R. Willinger, B. M. Diaw, and H. S. Kang, "Finite element modelling of skull fractures caused by direct impact," *International Journal of Crashworthiness*, vol. 5, no. 3, pp. 249–258, 2000.

[47] D. Willinger, R. and Baumgartner, "Numerical and physical modelling of the human head under impact – toward new injury criterion," *International Journal of Vehicle Design 32(1-2)*, 2001.

[48] R. Willinger and D. Baumgartner, "Human head tolerance limits to specific injury mechanisms," *International Journal of Crashworthiness*, vol. 8, no. 6, pp. 605–617, 2003.

[49] C. Deck and R. Willinger, "Improved head injury criteria based on head FE model," *International Journal of Crashworthiness*, vol. 13, no. 6, pp. 667–678, 2008.

[50] V. L. McElhaney, J. H., Mate, P. I. and Roberts, "A new crash test device– "Repeatable Pete"," in *Proceedings of 17th Stapp Car Crash Conference*, 1973.

[51] H. and Ono, K., Kikuchi, A., Nakamura, M., Kobayashi and H. Nakamura, "Human head tolerance to sagittal impact reliable estimation deduced from experimental head injury using sub-human primates and human cadaver skulls," in *Proceedings of 24th Stapp Car Crash Conference*, 1980.

[52] P. Löwenhielm, "Mathematical simulation of gliding contusions," *Journal of Biomechanics 8(6)*, 1975.

[53] B. Princemaille, Y., Trosseille, X., Mack, P., Tarriere, C. and B. F. and Renault, "Some new data related to human tolerance obtained from volunteer boxers," in *Proceedings of 33rd Stapp Car Crash Conference*, 1989.

[54] L. E. Margulies, S. S. and Thibault, "A proposed tolerance criterion for diffuse axonal injury in man," *Journal of Biomechanics 25(8)*, 1992.

[55] C. H. Hardy and P. V. Marcal, ""Elastic analysis of a skull,"," *Journal of Applied Mechanics*, vol. 40, no. 4, pp. 838–842, 1973.

[56] T. Shugar, "Transient structural response of the linear skull-brain system." 1975.

[57] V. H. K. Goldsmith and W., ""Dynamic loading of a fluid-filled spherical shell,"," *International Journal of Mechanical Sciences,*, vol. 14, no. 9, pp. 557–568, 1972.

[58] T. B. K. Hubbard and R. P., ""Parametric study of head response by finite element modeling,"No Title," *Journal of Biomechanics*, vol. 10, no. 2, pp. 119–132, 1977.

[59] H. S. Chan, ""Mathematical model for closed head impact,"." 1974.

[60] R. Hosey, *"A homeomorphic finite element model of the human head and neck,"*. PhD thesis, 1982.

[61] J. Yang, J. Dai, and Z. Zhuang, "Human Head Modeling and Personal Head Protective Equipment: A Literature Review," *Lecture Notes in Computer Science (including subseries Lecture Notes in Artificial Intelligence and Lecture Notes in Bioinformatics)*, vol. 5620 LNCS, pp. 661–670, 2009.

[62] J. S. Ruan, T. B. Khalil, and A. I. King, "Finite element modeling of direct head impact," *SAE Technical Papers*, 1993.

[63] T. B. K. C. Zhou and A. King, ""A new model comparing impact responses of the homogeneous and inhomogeneous human brain,"," in *Proceedings of 39th Stapp Car Crash Conference*, (San Diego), 1995.

[64] T. B. K. L. Zhang, K. H. Yang, R. Dwarampudi, K. Omori, T. Li, K. Chang, W. N. Hardy and A. I. King, ""Recent advances in brain injury research: a new human head model development and validation,"," in *Proceedings of 45th Stapp Car Crash Conference*, (San Antonio), 2001.

[65] W. H. A. I. King, K. H. Yang, L. Zhang and D. C. Viano, ""Is head injury caused by linear or angular acceleration?,"," in *Proceedings of International IRCOBI Conference on the Biomechanics of Impacts*, (Lisbon), 2003.

[66] B. Kang, H. S., Willinger, R., Diaw, B. M. and Chinn, "Modeling of the human head under impact conditions: a parametric study.," in *Proceedings of 41st Stapp Car Crash Conference*, 1997.

[67] D. Marjoux, D. Baumgartner, C. Deck, and R. Willinger, "Head injury prediction capability of the HIC, HIP, SIMon and ULP criteria," *Accident Analysis and Prevention*, vol. 40, no. 3, pp. 1135–1148, 2008.

[68] L. Taleb and C. M. Kopp, "of Head Mathematical Models," vol. 12, no. 4, pp. 743–754, 1995.

[69] S. K. Hardy and W. N., ""Correlation of an FE model of the human head with local brain motion-consequences for injury prediction,"," in *Proceedings of 46th Stapp Car Crash Conference*, (Ponte Vedra, USA), 2002.

[70] T. J. Horgan and M. D. Gilchrist, "The creation of three-dimensional finite element models for simulating head impact biomechanics," *International Journal of Crashworthiness*, vol. 8, no. 4, pp. 353–366, 2003.

[71] A. M. Nahum, R. Smith, and C. C. Ward, "Intracranial pressure dynamics during head impact," *SAE Technical Papers*, 1977.

[72] M. C. Ueno, K., Melvin, J. W., Lundquist, E. and Lee, "Ueno, K., Melvin, J. W., Lundquist, E. and Lee, M. C.," *American Society of Mechanical Engineers (ASME), Applied Mechanics Division (AMD)*, no. 106, pp. 123–124, 1989.

[73] A. I. Ruan, J. S., Khalil, T. and King, "Human head dynamic response to side impact by finite element modeling.," *J Biomech Eng 113*, pp. 276–283, 1991.

[74] R. Willinger, H. S. Kang, and B. Diaw, "Three-dimensional human head finite-element model validation against two experimental impacts," *Annals of Biomedical Engineering*, vol. 27, no. 3, pp. 403–410, 1999.

[75] S. H. Shuck, L. Z. and Advani, "Rheological response of human brain tissue in shearing.," *J. Basic Eng*, no. 94, pp. 905–911, 1972.

[76] Z. S. Liu, X. Y. Luo, H. P. Lee, and C. Lu, "Snoring source identification and snoring noise prediction," *Journal of Biomechanics*, vol. 40, no. 4, pp. 861–870, 2007.

[77] R. L. Stalnaker, *Mechanical properties of the head.* Phd dissertation., West Virginia University., 1969.

[78] F. A. Yoganandan, N., Li, J., Zhang, J. and Pintar, "Role of falx on brain stress-strain responses. In: Kamkim, A. and Kiseleva, I. (Eds.)," *Mechanosensitivity of the Nervous System.*, pp. 281–297, 2009.

[79] R. Turquier, F., Kang, H. S., Trosseille, X., Willinger and A. Trosseille, X., Lavaste, F., Tarriere, C. and Domont, "Validation study of a 3D finite element head model against experimental data.," in *Proceedings of 40th Stapp Car Crash Conference,*, (Albuquerque, USA), pp. 283–293, 1996.

[80] O. Jiroušek, J. Jíra, J. Jírová, and M. Micka, "Finite element model of human skull used for head injury criteria assessment," *Solid Mechanics and its Applications*, vol. 124, pp. 459–467, 2005.

[81] L. Zhang, K. H. Yang, and A. I. King, "Comparison of brain responses between frontal and lateral impacts by finite element modeling," *Journal of Neurotrauma*, vol. 18, no. 1, pp. 21–30, 2001.

[82] A. S. Al-Bsharat, *Computational analysis of brain injury.* Phd dissertation, Detroit: Wayne State University., 2000.

[83] A. Zhou, C., Khalil, T. B. and King, "Viscoelastic response of the human brain to sagittal and lateral rotational acceleration by finite element analysis.," in *Proceedings of International IRCOBI Conference on the Biomechanics of Impacts,*, pp. 35–48, 1996.

[84] T. N. E. Wang and R. Rauch, ""Back to elements-tetrahedra vs. hexahedra,"," in *Proceedings of the 2004 international ANSYS conference,*, 2004.

[85] G. F. d. J. Migueis, "Simulação numérica da ocorrência de hematomas," 2018.

[86] J. M. C. Costa, "Desenvolvimento de um modelo pormenorizado," 2019.

[87] A. Barbosa, "Development of a computational model of the human skull," 2020.

[88] F. A. O. Fernandes, R. J. Alves de Sousa, and M. Ptak, "Head Injury Simulation in Road Traffic Accidents," *Springer Briefs in Applied Sciences and Technology*, 2018.

[89] R. W. Ogden, "Large Deformation Isotropic Elasticity - on the Correlation of Theory and Experiment for Incompressible Rubberlike Solids.," 1973.

[90] K. Miller and K. Chinzei, "Mechanical properties of brain tissue in tension," *Journal of Biomechanics*, vol. 35, no. 4, pp. 483–490, 2002.

[91] B. Coats and S. S. Margulies, "Material properties of porcine parietal cortex," *Journal of Biomechanics*, vol. 39, no. 13, pp. 2521–2525, 2006.

[92] D. C. Lin, D. I. Shreiber, E. K. Dimitriadis, and F. Horkay, "Spherical indentation of soft matter beyond the Hertzian regime: Numerical and experimental validation of hyperelastic models," *Biomechanics and Modeling in Mechanobiology*, vol. 8, no. 5, pp. 345–358, 2009.

[93] B. Rashid, M. Destrade, and M. D. Gilchrist, "Mechanical characterization of brain tissue in compression at dynamic strain rates," *Journal of the Mechanical Behavior of Biomedical Materials*, vol. 10, pp. 23–38, 2012.

[94] A. Yang, K.H. and King, ""Modeling of the brain for injury simulation and prevention"," *Biomechanics of the Brain,*, pp. 99–110, 2011.

[95] W. N. Hardy, C. D. Foster, M. J. Mason, K. H. Yang, A. King, and S. Tashman, "Investigation of Head Injury Mechanisms Using Neutral Density Technology and," *Stapp car crash journal*, vol. 45, no. November, 2001.

[96] D. Systemes, ""Explicit dynamic analysis",." `https://abaqus-docs.mit.edu/2017/English/SIMACAEANLRefMap/simaanl-c-expdynamic.htm`. Accessed: August 2022.

[97] G. Reader, ""Graph reader",." `http://www.graphreader.com/`. Accessed: August 2022.